Doctoral Dissertation

Relaxation in artificial atomic structure and anisotropic migration on Si surface

University of Tokyo
Department of Superconductivity

January 1996

Taro Hitosugi

(1)

Doctoral Dissertation

Relaxation in artificial atomic structure and anisotropic migration on Si surface

University of Tokyo

Department of Superconductivity

January 1999

Taro Hitosugi

博士論文

シリコン表面上における人工原子構造の緩和と異方的原子拡散

東京大学大学院 工学系研究科

超伝導工学専攻

1999 年 1 月

一杉 太郎

Preface

The world is changing quite rapidly. Developments in information technologies, based on recent progress in semiconductor technology, accelerate the dramatic changes in our life. "Nanotechnology" explores the fundamental physics and engineering of nanometer to atomic-scale solid state materials. The nanotechnology will provide us of much powerful computing environment, ultra-high density storage system, and etc.

In recent years, rapid progress has been made in the controlled and reproducible manipulation of atoms with the scanning tunneling microscope (STM). The atom manipulation is very promising technique in both scientific and engineering points of view. It is quite promising that many new physics will be found in artificial atomic structures and contribute to our future daily life.

In order to investigate atomic-scale devices, we need to design appropriate device structures and materials as well as to improve atomic-scale fabrication techniques. A Si(100) surface is especially important in these days because it is used for fabricating semiconductor devices. When miniaturization of structures in semiconductor devices proceeds, nanoscopic understanding of this surface becomes more important. Since the trend of miniaturization is an essential stream in electronics, nanotechnology on this surface is now attracting intensive attentions.

The purpose of this study is to obtain guidelines for fabrication of conducting atomic wires. In this dissertation, characteristics of atomic-scale structures are first discussed. There are many studies on fabrication of atomic structures, however, the characterizations of the structures are still unexplored. The atomic-scale dangling-bond (DB) structures on a hydrogen-terminated Si(100)2×1 surface is discussed based on STM results and first-principles calculations. We concluded that length and width of the DB structrures sensitively affect the electronic structures in the atomic-scale DB structures. This DB structure itself may be too reactive chemically to use in practical atomic-scale devices, however, we think that it serves as an instructive example of an atomic-scale structure on a semiconducting surface.

Further, atomic-scale migration path of adsorbate atom is discussed. More detailed studies on migration are demanded from the fabrication of films and atomic structures. Atomic-scale surface migration of a Ga atom on a hydrogen-terminated Si(100)2×1 surface is studied using STM and first-principles calculations. Quantitative studies of adsorption free-enegy variation is possible using a Ga migration as a local probe. We point out that the migration path may be varied by the sub-surface defects.

This dissertation is organized as follows. In Chapter 1, the motivations and backgrounds of this study are briefly described. Miscellaneous topics related to this dissertation are introduced in Chapter 2. Detailed descriptions of our new STM and procedures of experiments are presented in Chapter 3. The experimental results are presented and discussed in Chapter 4, and finally, in Chapter 5, comprehensive conclusions and state future prospects of this study are presented. In this dissertation, I invite the reader to the entrance of vast new nanometer/angstrom world filled with curious physics.

List of abbreviations

DB	dangling bond
DBs	dangling bonds
DOS	density of states
FIM	field ion microscope
LDA	local density functional approach
LDOS	local density of states
LT	low temperature
PC	personal computer
PES	potential energy surface
RT	room temperature
SPM	scanning probe microscopy
STM	scanning tunneling microscopy
STS	scanning tunneling spectroscopy
UHV	ultra high vacuum
E_F	Fermi energy
I_t	tunneling current
V_s	sample bias voltage
1D	one dimensional

Contents

Chapter 1

Motivations

Physics in nanometer-scale structure has been attracting much attention, since the minimum structure in semiconductor devices are in a few hundreds of nanometer region. Even if the physical properties of a particular structure are well known for a size of the order of 10 nm or larger, its properties may be greatly altered if its size is reduced to an atomic scale. Many of the physical and chemical limits in miniaturization are pointed out and proposals of new devices are urgent issues. *The motivation of this dissertation is to study physics in atomic level in order to obtain guiding principles for designing materials and structures of atomic-scale devices.*

The future goal of this study is to fabricate conducting atomic-scale wire, contacted with macroscopic leads. The major questions related to this goal, which is discussed in this dissertation are:

1. *How does an atomic-scale structure relax. Which atomic configuration does the atomic structure have finite density of state (DOS) at the Fermi energy (E_F).*
   Even if there is a method to fabricate atomic-scale structure, the stabilization of the structure may lead to semiconducting properties and may hinder the electronic conduction. Understanding the atomic-scale relaxation is essential in fabricating any atomic-scale structure.

2. *How does an adsorbate atom migrate in atomic scale.*
   A selective deposition is the most promising process in fabricating atomic structures. Nanoscopic observations of adsorbate migration, determined by the adsorption potential energy surface (PES), is unexplored. To understand migration and growth at atomic scale is also motivated by requirements on ultra-high quality thin films.

We used an elegant and sophisticated tool, the STM, to investigate the above open questions. In recent years, rapid progress has been made in manipulating atoms with the STM. This high-resolution experimental techniques enable us to study the various behaviors of atoms and electronic properties in atomic structure.

In this chapter, I will briefly describe the main backgrounds of this study.

1.1 Limits in miniaturization of semiconductor device

Advances of semiconductor science and technology have propelled drastic revolution in our life. It is no doubt that the digital technologies have improved our life and the world economy. High-speed digital processing, high-speed digital communication, and ultra-high density storage are the key technology of the coming "information century." Recently, electronic money and electronic commerce has been in great advance. The deregulation in financial market, so called as "Big bang" is also a result of development of information technology. All these evolutions are due to the continuous progress in semiconductor science and technology.

Figure 1.1 shows the size of minimum structures in DRAM (dynamic random access memory) at the production level. The miniaturization and performance of a device proceed following the scaling rule [1, 2], in which all the dimensions are shrunk by a "scaling factor." The performance of semiconductor devices doubles every 18 months and this trend of development seems continuing still in early 21st century. An existing patterning technology beyond 0.1 μm is a direct electron-beam writing. However, Semiconductor Industry Association's (SIA) *National Technology Roadmap for Semiconductors* (finalized in 1998) [3] claims that still at this stage in 1999, there is no known solution to fabricate devices, at application level, which have a feature size of 130 nm and smaller. A number of post-optical technologies show promise, however, no single technology has yet become clear choice. We may face the limit of conventional semiconductor devices in 10 to 20 years (that is, 2010 to 2020!).

Besides the limits in fabrication processes, it is said that there exist many physical limitations [4, 5]. Examples are:

1. Physics in low-dimensional system become dominant when the miniaturization proceeds. These phenomena alter the physics in conventional semiconductor devices.

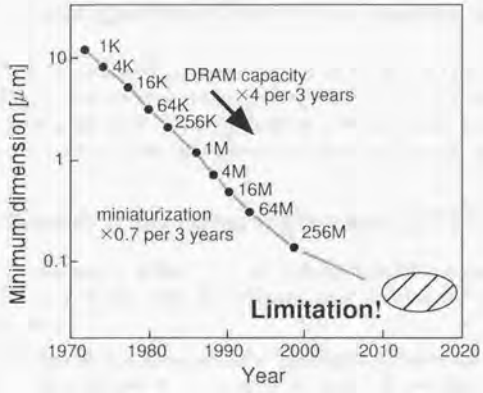

Figure 1.1: Miniaturization of DRAM. The integration doubles every 18 months.

2. Presence or absence of individual atoms, as well as their behavior (diffusion), will become significant. A statistical error of the dopant distribution in a small doping area, lead to fluctuation of device performances.

3. Insulator tunneling may become apparent below the insulator thickness of 4 nm.

4. Heat dissipation becomes problem when integration proceeds. Devices become too high temperature that the devices are destroyed by the heat.

From the above reasons, new devices, such as quantum effect devices [6, 7] and single electron transistor [8], have recently been attracting much attentions as candidates to replace silicon integrated cicuit devices.

Those new devices are fabricated by the present semiconductor lithography techniques. These methods are called 'top down,' which is to fabricate devices by repeating etching and deposition processes. Another fabrication technique called 'bottom up,' which is to compose and array atoms one by one, is another way to realize new devices. In the next section, the 'bottom up' fabrication techniques using STM are briefly reviewed.

1.2 Investigation of artificial atomic structures

An STM has become indispensable apparatus to manipulate atoms one by one, and has opened up important new fields in both science and technology. In the following sections, fabrication of atomic structures using STM and attempt to characterize the fabricated structures are briefly reviewed.

1.2.1 Scanning tunneling microscope (STM)

An STM [9] can image surface of a conducting material on an atomic scale. Detailed reviews of this elegant technique and theories are described elsewhere [10, 11].

The high spatial resolution of the STM originates from the extreme sensitivity of a tunneling current to change in a tip-sample distance. A sharpened STM tip, tungsten in this study, is brought to approximately 1 nm from a surface under investigation. The wavefunctions of the STM tip and the surface overlap at such distances, allowing the tunneling current to flow between them. The tunneling current predominantly flows through the tip apex atoms that are closest to the sample surface, yielding high lateral and vertical resolution. For typical values of work functions, typically 4 eV, the tunneling current changes by almost an order of magnitude for a change in a tip-sample distance of only 0.1 nm (1 Å).

A positive bias voltage applied to a sample (V_s>0) allows electrons to flow from filled state on an STM tip to empty state on the sample. For simple metals, there is typically no strong variation of the local density of states (LDOS) near E_F. As a result this polarity provide information on empty-state LDOS of the sample [11]. When a negative bias voltage is applied to a sample (V_s<0), the STM can extract information on filled-state LDOS of the sample.

An STM image contains information on surface topography, LDOS, and time average of those two factors. Further, the STM image reflects the convoluted information on an STM tip and a surface. In the constant-current imaging mode, these information are reflected by variations of an STM tip height position. Consequently, *the STM does not necessarily reveal the positions of surface atoms*. For example, the charge transfer between sites will cause the filled and empty states to localize in different regions in unit cell, such as in GaAs(110) surface [12]. On those surfaces, the STM images change depending on the polarity of bias voltages, and the images do not correspond to the positions of surface atoms.

An important feature of the STM is the ability to perform scanning tunneling spectroscopy (STS). The data are obtained by positioning an STM-tip at a fixed height above the surface and recording the change of a tunneling current (I_t) as a sample bias voltage (V_s) is swept within some range near E_F. The measured conductance ($\mathrm{d}I_t/\mathrm{d}V_s$) roughly correspond to the LDOS of the sample [11]. This requires that the STM tip DOS does not strongly vary or exhibit pronounced structure over the energy range of the spectrum.

In order to construct surface structure or surface charge distribution from STM images, theoretical calculations play an essential role. Almost any of the STM data needs to be supported by the theoretical calculations, since what STM observe is a time average of the very local charge distribution.

There exist many techniques related to scanning probe microscopy (SPM), such as, atomic force microscope (AFM), scanning SQUID microscope, magnetic force microscope (MFM), and etc [13]. The ability of scanning probe microscopes (SPMs) to image and manipulate matter on the nanometer scale made clear that SPMs have a potential as a tool to fabricate nanoscale devices. The studies using SPM will surely increase in the future.

1.2.2 Fabrication and characterization of atomic structures

Long before the invention of the STM, in 1959, Richard Feynman gave a visionary speech entitled "There's Plenty of Room at the Bottom," inviting scientists to enter a new field of physics, a world in which devices would be constructed out of components each made of only a few hundred atoms or even made of single atoms [14].

As one example, he considered what would happen if bits of information could be stored in a cubes of $5\times5\times5$ atoms, that is, a cluster of 125 atoms. He concluded that if these bits of information could be stored in a three-dimensional array, the contents of all the books in all the national libraries around the world (some 10^{15} bits according to his estimation in 1959), could be stored in a volume of a size of a dust!

A controlled fabrication and characterization of atomic structures *on silicon surface* will facilitate the fabrication of new types of electronic devices. In particular, nanowires [15] have attracted considerable attention. From a technical point of view, it is used as a conducting wire in semiconductor devices. On the other hand, from a scientific point of view, such small a one-dimensional (1D) structures are expected to exhibit intriguing physical properties, such as a quantized conductance [16] or a transition to Tomonaga-

Luttinger liquid [17] at low temperature.

In order to investigate these devices we need to design appropriate device structures and materials as well as to improve atomic-scale fabrication techniques. On metallic substrates, the 1D electronic states of such structures are usually strongly mixed with the bulk metal states. In order to study unperturbed 1D effects, semiconducting or insulating material should be used as substrate.

The challenge therefore is to *fabricate an atomic-scale metallic wire on a semiconducting substrate*. Recently, *not only fabricating atomic structures but also characterizing the physical properties of those structures have been key issues*. Our attempt to measure STS of atomic structure and investigate electronic properties is also along this direction.

In this section, I briefly review the fabrication using STM and the characterization of atomic structures.

Fabrication of nanostructure

The idea of manipulating atom one by one was realized not so after the invention of STM. Thorough reviews of this field can be found elsewhere [18-20].

An interaction between an adsorbate and an STM tip can be controlled, and is used to manipulate atoms. The first demonstration of a controlled atomic manipulation with an STM was the deposition of a single Ge atom onto a Ge(111) surface from an STM tip in 1987 [21]. The most beautiful demonstration of a controlled atomic-scale fabrication was accomplished by Eigler *et al.*, using a very stable STM operated at 4 K. They laterally manipulated Xe atoms adsorbed on a Ni(100) surface, and assembled structures [22]. Subsequently, they moved atoms of Pt and Fe and molecules of CO on various metal surfaces [23].

For the investigation of nanoelectronic devices and model systems, an important aspect of the fabrication methods is the ability to produce atomically ordered structures of desired geometry. The manipulations on surface include deposition, desorption, and lateral sliding of atoms. Combinations of these atom manipulation processes and selective adsorbate deposition potentially can be used to assemble arbitrary structures or to add components to previously fabricated structures. The four main categories of fabrication by using the STM, and related studies are:

1. Arrange adatoms into a pattern by sliding the atom.

(a) Many examples of lateral atomic manipulation have been accomplished, such as: displacing adsorbed Si atoms on Si(111) and Cl on Si(100) [24], and moving vacancies on GaP(110) [25]. In some cases nanoscale structures have been assembled: by forming 1D islands of Cs atoms on GaAs(110) [26] and by accumulating Si atoms under the STM tip to create nanocolumns [27, 28].

(b) Pushing or pulling the adsorbates were distinguished by monitoring an STM tip height while sliding the atoms [29].

2. Patterning by depositing atoms onto the surface from an STM tip or by decomposing precursor gaseous molecules.

   (a) Clusters of atoms from a gold STM tip were reliably deposited onto various surfaces by Mamin *et al.* in 1990 [30]. The fabricated mounds had a narrow distribution of sizes and were created at evenly spaced positions to write nanoscale patterns.

   (b) Structures, 10 - 30 nm in size, were fabricated using organometallic gases [31] and using aqueous silver fluoride [32].

   (c) Individual atoms of hydrogen were deposited onto Si(111)7×7 surfaces from a Pt/Ir tip [33]. The hydrogen atoms were supplied from surrounding H_2 gas.

   (d) Si atoms were extracted and redeposited on a Si(111)7×7 surface [34, 35].

3. Use an STM to create an etch mask (not atomic scale but nanometer scale).

   (a) Pattern generation on silicon by exposure of resist [36].

   (b) Chemical modification of hydrogen-terminated Si(111) surface and selective etching [37].

   (c) An array of GaAs dots were grown using nitrided mask on GaAs [38].

4. Define mask patterns using desorption of atoms from the surface. The atomic structure is fabricated with subsequent selective deposition.

   (a) Hosoki *et al.* removed individual S atoms in rows from MoS_2 surface at room temperature in ambient air [39].

   (b) Individual hydrogen atoms are desorbed from a hydrogen-terminated Si(100)2×1 surface, and patterning of DB (DB structure) was demonstrated [40].

(c) Hashizume *et al.* reported on the formation of atomic-scale Ga structures on this surface using DB wires [41]. Details are described later in this section. Fe [42], Al [43], and Ag [44] wires are fabricated using the same principle. Further, selective deposition of O [45, 46] is studied.

In order to connect atom manipulation techniques to applications, *the most promising substrate is silicon*. A hybrid structure, made from present semiconductor lithography techniques and atom manipulation techniques, is the most visionary way for the application. The advantages of studying Si(100)2×1 surface are summarized as follows:

From an engineering point of view:

- Most of the semiconductor devices are formed on the Si(100) surface. The nanofabrication techniques can be applied to the fabrication of semiconductor devices (hybrid device).

From a scientific point of view:

- Hydrogen atoms on a hydrogen-terminated Si(100)2×1 surface can be desorbed by using an STM [40]. The desorption leaves Si atom with one DB on the surface. In this way, DB structure can be fabricated by patterning dangling bonds (DBs).
- Atomically flat surface is routinely obtained.
- Bulk conductivity can be reduced enough for characterizing physical properties of the atomic structures. This is accomplished by using a low dopant-level sample and/or by reducing temperature of the sample.
- Surface states resulted from the DBs of the Si dimers can be passivated by hydrogen adsorption.
- A hydrogen-terminated surface is less reactive and can be kept clean even for several days in UHV.
- Reactivity to some of the metal atoms are low and the surface mobility of those metal atoms are expected to be high on a hydrogen-terminated surface. A DB structure is more chemically reactive than hydrogen-terminated surface, in general. Consequently, selective adsorption onto the DB structure is possible.

Hashizume *et al.* reported on the formation of atomic-scale Ga wires on a hydrogen-terminated Si(100)2×1 surface. A Ga atom wire was fabricated by depositing Ga atom after fabricating a DB wire [41]. At room temperature, deposited Ga atoms are mobile on hydrogen-terminated surface and desorb only to DBs. The Ga adsorbate is stabilized by more than 1 eV on the DB site [47]. Figure 1.2 shows the STM image of fabricated Ga wire and its ball-stick model. Width of the Ga wire is one to two atoms, and the length is more than 10 nm. The difference between the DB wire and the Ga wire observed in STM image is their height. The Ga wire has a height of about 0.3 nm, but the DB wire has only approximately 0.1 nm. Whether this Ga wire is electrically conducting or not is a very interesting problem.

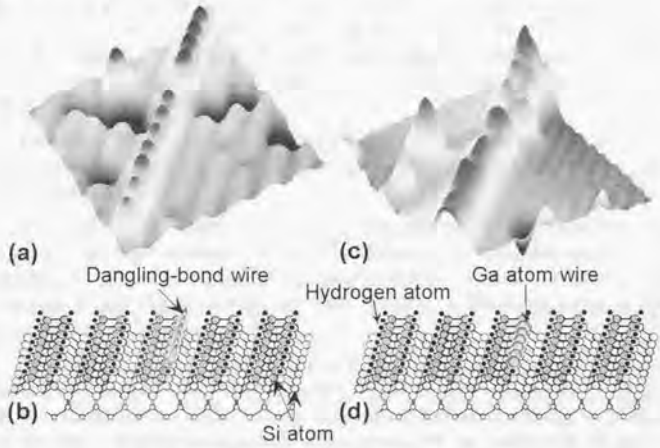

Figure 1.2: Fabrication of Ga atom wire on hydrogen-terminated Si(100)2×1 surface. (a) and (b) show the three-dimensional STM image of DB wire and its ball-stick model, respectively. (c) and (d) show the Ga wire and its ball-stick model, respectively. The Ga atom wire was fabricated by depositing Ga atom after fabricating DB wire. The Ga wire is observed higher than the DB wire. Note that STM images are from different sample areas.

Characterization of nanostructure

There are only a few experimental results on the characterization of physical properties, concerning artificial atomic structures.

The first characterization of an artificial atomic structure and its effect to a substrate are studied by Crommie *et al.* They measured a tunneling spectroscopy of artificial Fe corral on Cu(111) [48], and observed the wave nature of electrons directly from standing-wave patterns spatially resolved on the Cu surface. A surface resistivity was measured using artificially fabricated insulating trenches on a Si(111)7×7 surface by Heike *et al.* [49]. Aono *et al.* developed 'photon STM,' an STM combined with photon multiplier, and detected the photon from a artificial DB structure on a hydrogen-terminated Si(100)2×1 surface [50]. Photon STM and spin-polarized STM are the examples of approaching physical properties in nanoscale structure using SPM techniques. Attempts to characterize artificial atomic structures will certainly increase in the near future.

There are several theoretical results which predict properties of atomic wires by using the first-principles calculations based on a local density functional approach.

Watababe *et al.* studied electronic structures of DB wires and Ga-atom wires on a hydrogen-terminated Si(100)2×1 surface by using the first-principles calculations [51]. The Ga-atom wire was found to be semiconductive at the coverage of one Ga atom per one DB. Further, a ferromagnetism in this Ga-atom wire is pointed out [52].

Haye *et al.* investigated Na-doped DB wire on a hydrogen-terminated Si(100)2×1 surface [53]. They reported that in low coverages, Na atoms simply act as electron donor. This results in unfilled surface band, as a result, the metallic behavior is expected. First-principles calculations by Brocks *et al.* show that a linear chain of Al atoms on Si(100) is semiconducting [54].

Besides on Si surface, Lang calculated a resistance of atomic wire connecting two semi-infinite metallic electrodes [55, 56]. Calculated length-dependent resistance is very interesting. Band structures of a 1D atomic chain, two-dimensional square array, and two parallel atomic chains are calculated for various atoms as a function of lattice constant using tight-binding theory with universal parameters [57].

Bouju *et al.* studied Au atomic wires on NaCl surface [58]. According to their molecular-dynamics calculations, a single-atom row of gold on a NaCl substrate was found to be unstable, while a gold wire with much larger width is apparently stable. von Allmen *et al.* studied Si atomic wire [59].

As described above, atomic wires on semiconductor surfaces reveal the possibility to exhibit a wide variety of physical properties. However, there are only a few experimental results on characterization of the atomic structures, so far.

Some studies aim contact to atomic structures. One of the attempts is to use bonding pad which is fabricated by using mask [60, 61]. Another approach is to construct an STM which has multiple STM tips [61, 62]. The individually movable STM tips are to be contacted to the nanowire for two-point or four-point resistivity measurement. In these way, high-resolution experimental techniques for determining the electronic properties of atomic structures will be possible. Whether atomic structures are electrically conductive or not is very interesting issue.

Nothing is known about a contact between macroscopic structure and nanostructure. A study of contact was the first step to understand semiconductor physics. Later on, junction became important element for semiconductor devices. I am quite confident that the contact between a macroscopic structure and a nanostructure will be a treasure box of new physics [63].

Chapter 2

Introduction

This chapter describes the miscellaneous basic understanding of this study.

2.1 Principles of Si(100) surface relaxation and reconstruction

Fundamental principles related to relaxation and reconstruction on Si surfaces are briefly introduced in this section. When a surface forms, interactions among atoms in the first-layer and sub-layer atoms are modified, due to the absence of neighboring atoms on one side. In order to reach a new equilibrium configuration, the rearrangements/displacements of the atoms occur. The arrangements may result in a pure compression or expansion of inter-plane separations of the surface layers. This process is called surface relaxation. Surface relaxation does not necessarily induce a change in the surface periodicity. Surface reconstruction refers to a more complicated phenomenon in which atomic rearrangements introduce a lateral change in the surface periodicity and simultaneous relaxation as well. In this dissertation, *the term "relaxation" is used as a displacements of the atoms in order to gain total energy of the system.*

The inter-atomic bonds in Si are tetrahedral due to the hybridization of atomic orbital, which is referred to as sp^3 hybrid bond. This directional covalent bond determine the structure of bulk Si and Si surface. There are two spin-paired electrons on each inter-atomic bond. On formation of a surface, at least one bond for each atom is cut, producing dangling bonds (DBs). The lack of electron pairing makes these DBs energetically unstable, and results in a large free energy. The surface atoms, thus, rearrange to minimize the number of the DBs. In this way, the free energy of the system

reaches its minimum.

On the non-relaxed Si(100) surface, each Si atom has two DBs. There is no advantage for the DBs to be in the original sp^3 hybrid orbitals. It is energetically favorable to dehybridize this configuration back into its original s and p orbitals. It is now well established that this surface forms a 2×1 reconstruction [64, 65]. Si dimers are formed between neighboring Si atoms along the $\langle 110 \rangle$ direction in order to reduce the number of unsatisfied DBs. As a result, each Si atom has a single DB on the reconstructed surface.

Orbital dehybridization is an important mechanism in covalent semiconductor reconstructions. In the simplest image, the surface 'buckles' as atoms alternately rise above and sink below the surface plane. The dehybridization triggers this motion and the sp^3 hybrid orbital is altered to the original s ($|s\rangle$) and p ($|p\rangle$) components.

Haneman discussed the electronic energy when the angle between the dangling bond (DB) and back bond (defined as Θ in Fig 2.1(a)) is altered [66]. The DB orbital $|\mathrm{D}\rangle$ can be expressed as following equation.

$$|\mathrm{D}\rangle = \sin\theta|s\rangle + \cos\theta|p_z\rangle \tag{2.1}$$

The axes and subscripts are defined as shown in Fig. 2.1. The angle θ characterizes the DB orbital. When θ changes from $\theta = 0$ to $\theta = \pi/2$, the DB orbital changes from a pure p orbital to a pure s orbital. Considering that the backbond orbitals $|\mathrm{B}_1\rangle$, $|\mathrm{B}2\rangle$, and $|\mathrm{B}_3\rangle$ are orthogonal each other and also orthogonal to the DB orbital, the relation between Θ and θ can be derived as following equation [67].

$$\cos\Theta = -\sin\theta/\sqrt{2+\sin^2\theta} \tag{2.2}$$

The buckling turns the Si atoms into different electronic configurations. It is summarized as:

- Si atom which *rise above* the surface plane (larger Θ)

  The DB orbital becomes $s-like$ orbital.

  Three backbonds become p^3-like bonds.

- Si atom which *sink below* the surface plane (smaller Θ)

  The DB orbital becomes $p-like$.

  Backbonds become flatter sp^2-like bonds.

Since an $s-like$ orbital has lower energy than that of a $p-like$, an electron is transferred from a DB of the latter to the former DB. This is how the total

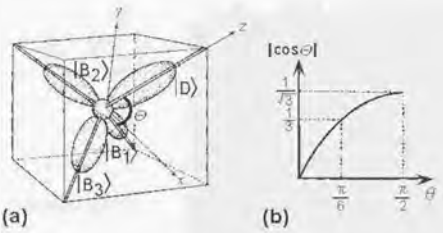

Figure 2.1: (a) Schematic view of the sp^3 hybrid orbital. The Θ is defined as the angle between dangling orbital $|\mathrm{D}\rangle$ and backbond orbital. (b) Plot of $|\cos\Theta|$ as a function of θ.

energy is lowered by the buckling. In this case, the resulting structures no longer are electronically degenerate.

The energy gain of the asymmetric buckling dimer on Si(100) surface is explained based on above discussions. Detailed discussions of general principles on relaxation and reconstruction can be found elsewhere [68, 69].

2.2 Si(100)2×1 surface

Intensive studies have been performed to understand the fundamental properties of a Si(100) surface, since most silicon devices are formed on this surface.

Schematic structure of the Si(100)2×1 surface and an STM image is shown in Fig. 2.2(a) and (b), respectively. An atomically flat terrace made of cocoon-shaped Si dimer is observed and dimer rows, made of Si dimers, are observed as bright lines running diagonally. The distance between adjacent dimers in a row is 3.85 Å, and the spacing between adjacent dimer rows is 7.7 Å. The dark spots on the surface correspond to Si defects.

The Si(100)2×1 surface consists of terraces separated by monoatomic steps (step height is 1.34 Å). The orientation of the dimer rows alternates between two perpendicular directions from one terrace to the next, because of silicon's diamond crystal structure.

Using tight-binding calculations, Chadi [70] pointed out the existence of buckled dimers. The first STM observations of the Si(100)2×1 surface by Tromp *et al.* revealed the presence of both buckled and unbuckled dimers [71]. The unbuckled dimer appears symmetric in STM image, but it is actu-

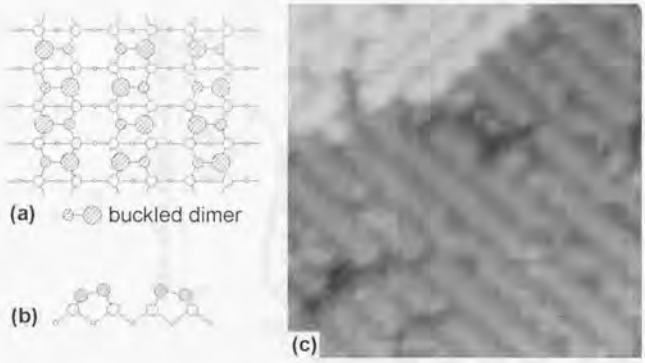

Figure 2.2: (a) Schematic view of a clean Si(100)2×1 surface. Hatched circles denote first-layer Si atoms. Large and small empty circles denote second- and third-layer Si atoms, respectively. (b) Schematic view of buckled dimers. (c) An STM image of clean Si(100)2×1 surface (8 nm×8 nm, V_s=-2.0 V, I_t=20 pA)

ally fluctuating between the two equivalent buckled configurations. Buckled dimers are observed only in the vicinity of defects and steps. Tromp suggested that dimers on this surface are dynamically buckled like flip-flop and that the observed symmetric dimer structure is a time average over two buckled configurations. The defects serve to pin the dimer in a buckled configuration [71]. Studies by Wolkow support this dynamic buckling model, and showed an increased number of buckled dimers at lower temperatures (below 120 K) that resulted in the formation of well-ordered c(4×2) domains [72].

Both photoemission and STS studies reveal the presence of an energy gap at E_F on a clean Si(100)2×1 surface. Fig. 2.3 shows the STS result obtained on a clean Si(100)2×1 surface at room temperature. The enegy gap and peak structures are consistent with the previous studies [73]. The normalized conductance shows a filled- and an empty-state peak located at 0.9 eV below and at 0.5 eV above E_F. These states are derived from the π interaction between the DBs of the Si atoms on a dimer and they represent the bonding and antibonding combinations, respectively [65, 73]. The calculated splitting between the band centers is reported to be approximately 0.7 eV [54].

Other possible explanations concerning the origin of energy gap are reported. In the buckled dimer case, it is due to the pair of surface states

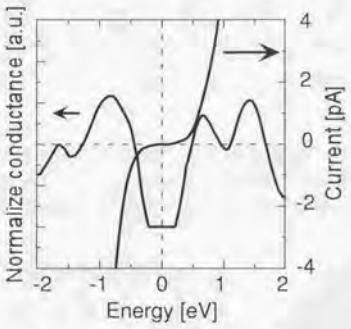

Figure 2.3: Normalized conductance curves and current-voltage (I_t-V_s) characteristics of clean Si(100)2×1 surface. The tunneling junction is stabilized at V_s=-2.0 V and I_t = 100 pA.

results from charge transfer between the DBs on the lower and upper atoms of the buckled dimer [74]. The electron correlation effects between electrons in DBs may be the origin of the energy gap [75]. The important fact is that the *DBs on the Si(100) surface are not independent but interact to reduce the surface free energy.*

At present, there is still controversy about the detailed structure of 2×1 surface [76]. Whether $c(4\times2)$ or $p(2\times2)$ has lower energy is still debated.

2.3 Hydrogen-terminated Si(100)2×1 surface

The hydrogen-terminated Si(100)2×1 surface has been studied extensively for many years. This surface is one of the most promising substrates for fabricating atomic-scale structures by extracting hydrogen atoms with an STM as described in section 1.2.2. There are three types of hydride structures on a Si(100) surface [77]: a monohydride with 2×1 symmetry (Fig. 2.4(a)), a dihydride with bulk-like 1×1 symmetry (Fig. 2.4(b)), and a mixed structure with alternate rows of monohydride and dihydride (3×1 symmetry) (Fig. 2.4(c)). In this study, the monohydride surface was used as a substrate.

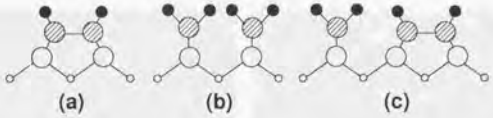

Figure 2.4: Schematic views of three types of hydride structures. (a) Monohydride. (b) Dihydride. (c) Trihydride. Hatched, filled, and blank circles denote, first-layer Si atoms, hydrogen atoms, and Si atoms, respectively.

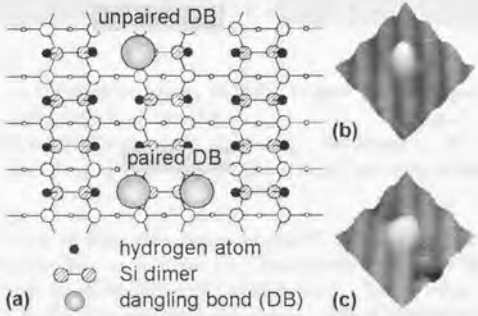

Figure 2.5: (a) Schematics of an unpaired and a paired DB on a hydrogen-terminated Si(100)2×1 monohydride surface. The blank circles (large and small) represent silicon atoms. (c) Filled-state STM image of an unpaired DB. Note that the peak is imaged off centered (on the left side) of a dimer row. (3 nm×3 nm.) (d) Filled-state STM image of a paired DB. The peak is imaged in center of a dimer row. (3 nm×3 nm).

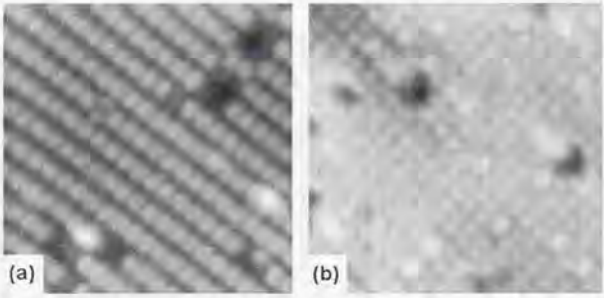

Figure 2.6: (a) Filled-state gray-scale STM image of a hydrogen-terminated Si(100)2×1 surface (96 K, 8 nm×8 nm, V_s = -2.0 V, I_t = 20 pA). White protrusions are DBs. (b)Empty-state gray-scale STM image (40 K, 7 nm×7 nm, V_s = -2.0 V, I_t = 20 pA). Note that STM images are from different sample areas.

An adsorption of atomic hydrogen to the Si(100)2×1 surface at approximately 650 K is known to yield the 2×1 monohydride surface [78]. Hydrogen atoms react with the DBs of the 2×1 surface but the dimer structure remains intact (Fig. 2.5(a)). The detailed preparation method is described in section 3.3.

Figure 2.6(a) shows a filled-state STM image of the hydrogen-terminated Si(100)2×1 monohydride surface. An atomically flat terrace made of cocoon-shaped hydrogen-terminated Si dimer is observed and dimer rows, made of Si dimers, are observed as bright lines running diagonally. The topographic maxima which appear as (white) protrusions in the gray-scale filled-state STM image are associated with DBs at the surface. The hydrogen-terminated dimers are observed to be approximately 0.1 nm lower in height than the DBs because the surface states of the Si dimers are passivated by hydrogen adsorption. The dark region on the surface correspond to missing-Si defects. Figure 2.6(b) shows the empty-state STM image of the hydrogen-terminated surface. A Si dimer appears to be two protrusions. The DBs still appear as protrusions in empty-state STM image.

The STM image in Fig. 2.6(a) is similar to that of a clean Si(100)2×1 surface, since the main part of the image is the cocoon-shaped Si dimer structure. On the clean Si(100) surface at room temperature, the buckled dimers are observed only near the steps and defects. On the contrary, no buckled dimer is observed on the hydrogen-terminated surface. Another important

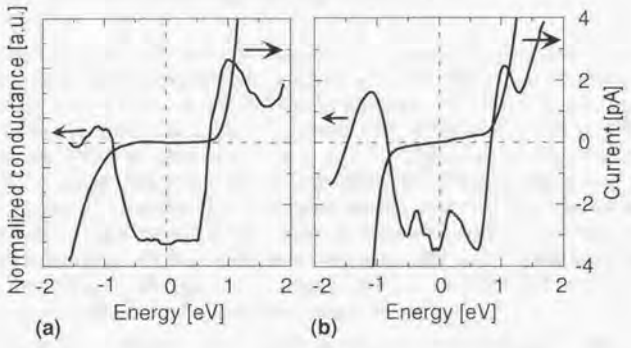

Figure 2.7: Normalized conductance curves and current-voltage (I_t - V_s) characteristics of (a) a hydrogen-terminated dimer and (b) an unpaired DB on a hydrogen-terminated Si(100)2×1 surface. The tunneling junction is stabilized at V_s = -2.0 V and I_t = 100 pA.

difference is the electronic structure of the surface.

In the case of the hydrogen-terminated surface, a wide band gap approximately 1 eV is observed (Fig. 2.7(a)). The energy gap is much larger on the hydrogen-terminated surface than on the clean surface (Fig. 2.3). The peak of the normalized conductance near +1.1 eV is assigned to antibonding states of the Si-H chemical bond [73]. The surface-state peaks observed on a clean Si dimer have disappeared due to the passivation by hydrogen atoms.

The DB structures on this surface are made up of two types of DBs, that is, unpaired and paired DB (Fig. 2.5(a)). One hydrogen atom desorbed from a Si dimer is called an unpaired DB [79], and it is imaged off-center on a dimer row (Fig. 2.5(b)). When two hydrogen atoms are desorbed from a Si dimer, it is called a paired DB. Since paired DB is imaged at the center of a dimer row (Fig. 2.5(c)), we can easily distinguish the unpaired and the paired DBs.

An isolated unpaired DB shows finite (non-zero) DOS at E_F and shows two DOS peaks at -0.4 and +0.2 eV (Fig. 2.7(b)). These peaks correspond to the DOS resulting from an unpaired DB state. An unpaired DB has a half-filled energy level and result in the finite DOS near E_F. These results agree well with those reported by Boland [73, 79].

2.4 First-principles calculations

In the STM study of solid surfaces, the first-principles calculation is an indispensable method to precisely analyze the experimental data. A synergism between the experiment and the theory tremendously improved our understanding. In many cases, an STM image reflects the time average of local electronic DOS, as described in section 1.2.1. Thus, the interpretation of an STM image should be carefully paid attention. Further difficulty is that the physical properties of a fabricated atomic structure can not be measured using conventional surface analysis methods, such as photoemission, atom diffraction, electron diffraction, and x-ray diffraction methods. These methods measure the spatially averaged information of the surface, and the fabricated structure is beyond their spatial resolution.

From above reasons, the comparison with the first-principles calculations become an essential tool to analyze STM images and STS data. We compared our STM/STS results with the first-principles calculations based on a local density function approximation (LDA).

The hydrogen-terminated Si(100)2×1 surface was represented by slab models containing five layers of Si atoms (Fig. 2.8(a)). The bottom surface was terminated with hydrogen, and the position of the bottom Si atoms are constrained to be in bulk like positions. The surface supercells used in the calculations are periodic 4×2 (Fig. 2.8(b)), 4×4, or 4×8 supercells. The repeated slabs are separated by a vacuum region of six times as long as the Si-Si atomic distance in the bulk Si crystal, that is, 13.974 Å.

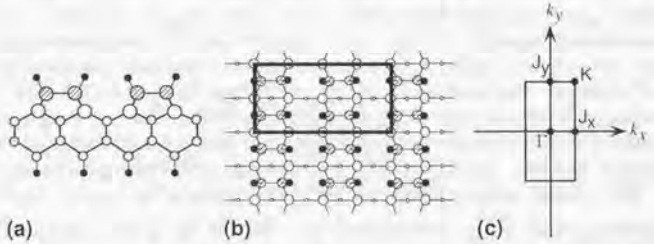

Figure 2.8: (a) A Slab model containing five layers of Si atoms. Hatched circles denote first-layer Si atoms. The blank and filled circles denote subsurface Si atoms and hydrogen atoms, respectively. (b) The schematic view of 4×2unit cell (c) Surface brillouin zone.

The experiments were compared with following calculations:

1. Electronic structure and relaxation of DB structure.

   Calculations by Watanabe *et al.* [51] using 4×2 unit cell.

2. Jahn-Teller distortion in DB structures.

   Calculations by Li *et al.* using 4×8 unit cell. Wave functions were expanded in a plane-wave basis set with an energy cutoff of 10 Rydberg (Ry).

3. Adsorption potential energy surface imaging.

   Calculations by Suwa *et al.* using 4×2 and 4×4 unit cell.

For an example, more details of calculation by watanabe *et al.* [80] are described. The optimized atomic geometry and electronic structures were calculated within a local density functional approach. The exchange correlation term used in the calculation was the Ceperley-Alder form [81] parametrized by Perdew and Zunger [82]. For electron-nuclei interaction, an ultrasoft pseudopotential proposed by Vanderbilt [83] was employed. The pseudopotential for H is generated in the electron configuration of $(1s)^{0.5}$, and only the s component was taken for the nonlocal part with one reference energy at the eigenvalue. The cutoff radii for the valence wave function (r_c^{WF}) and for the local potential (r_c^{pot}) were 0.8 and 0.7 a.u., respectively. For Si, the pseudopotential was generated in $(3s)^{1.25}(3p)^{1.75}$ configuration with $r_c^{WF} = 1.8$ a.u. and $r_c^{pot} = 1.6$ a.u., and s and p components were included with two and one reference energies, respectively. The second reference energy for the s component was 1.0 Ry above the eigenenergy. The charge augmentation functions were constructed using the method of Laasonen *et al.* [84] with cutoff radii of 0.7 a.u. for H and 1.6 a.u. for Si. Wave functions were expanded in a plane-wave basis set with an energy cutoff of 16 Ry. Two special k points were used for the integration in k space, which corresponds to a total of four k points in the whole first Brillouin zone. Both electronic and ionic degrees of freedom were optimized by using the coujugated gradient method [85].

In order to check the reliability of pseudopotential, the electronic structures and optimized geometries of H_2, SiH_4 molecules, and bulk Si were calculated. The atomic distances of each calculation and experimental value are shown in the Table 2.1.

The first-principles calculation based on the local density functional approach has some weak points. The calculated results tend to show smaller band gap than experimental results. In some cases, the calculated band

	Calculation	Experimental
H_2	0.768 Å	0.741 Å
Si-H in SiH_4	1.472 Å	1.480 Å
Si-Si in bulk Si	2.329 Å	2.352 Å

Table 2.1: Comparison of atomic distance. From ref. 80.

gap of bulk Si give a value of 0.52 eV, whereas an experimental observation shows 1.17 eV [86]. Considering these, a comparison of the energy gap with the experimental results shoud be carefully treated.

The first-principles calculations deal with infinite perfect DB wires and do not fully appreciate finite-length, disorder or electron correlation effects. Also, the effect of defect can not be considered. Even one impurity atom is introduced into the unit cell, it ends up with very high concentration due to the periodic condition. Since some types of defects extends over many lattice constants, these effects can not be treated using a first-principles calculations.

Chapter 3

Experimental

This chapter describes the details of the experimental methods used in this study. A ultrahigh-vacuum (UHV) low-temperature (LT) STM capable of atom manipulation was developed, and the manipulations of adsorbate atom were demonstrated. All the data presented in this study was obtained using this newly designed STM. After describing the design and operation of the new STM, procedures of preparing an STM tip and a sample are presented.

3.1 Development of UHV-LT STM

The possibility of carrying out STM measurement at low temperature [87] opens up many new fascinating world in fields such as surface imaging, tunneling spectroscopy, and atom manipulation. Followings are summary of several advantages to cool a sample and an STM tip to low temperature.

1. Cooling a sample decreases the amount of charge carriers in Si substrate, and can isolate a fabricated structure on a surface from a bulk. This isolation is required when measuring physical properties of a fabricated structure.

2. Frequency of a migration/diffusion event decreases to a observable time scale for STM observations. If the migration is suppressed, an atom manipulation can be possible in many combinations of adsorbate and substrate.

3. We found that a low tunneling current and a low bias voltage are required to desorb hydrogen atoms from a hydrogen-terminated Si(100)2×1 surface at low temperature, compared with those at room temperature.

Because of this low bias voltage and tunneling current, cooling a sample has advantages in desorbing hydrogen atom one by one in a controlled manner without damaging an STM tip. This fact results in the capability of fabricating precise DB structures.

4. Structural relaxation and phase changes can be studied, such as, Peierls transition, Mott transition, and etc. A thermal excitation can be controlled.

3.1.1 Design concept

Combining low temperature, UHV, and high-resolution STM is a difficult task because the requirements contradict each other. In UHV, gas thermal conduction can not be expected, and only thermal radiation and mechanical contacts are expected for the thermal conductivity. In order to cool a sample to low temperature, a good thermal conduction between a coolant and a sample is required. Increase of contacts between the coolant and the sample, however, lead to the increase of vibration transmission.

The developed STM is designed to achieve high-resolution STM image, and the lowest temperature achievable is the second aim. Considering manipulation of adsorbed atom and selective deposition, a deposition system must be installed.

A sample can be cooled down to 30 K. An STM tip and a sample are surrounded by 4-K copper walls, and they are suspended by four springs for vibration isolation. The suspension using springs efficiently damp acoustic noise, vibrational noise, and bubbling noise of liquid nitrogen. This spring suspension and eddy-current damping ensure high-resolution images even when liquid nitrogen is used for a coolant. Easy handling is another advantage of this STM. It takes less than 5 minutes to change a sample and an STM tip. The STM can operate more than 15 hours by one full liquid-helium transfer.

The performance of an STM control system is crucial to the resolution and stability of STM images. The STM measurement system is fully digitally controlled and the software is specially tuned up for atom manipulation.

Details are described in following subsections.

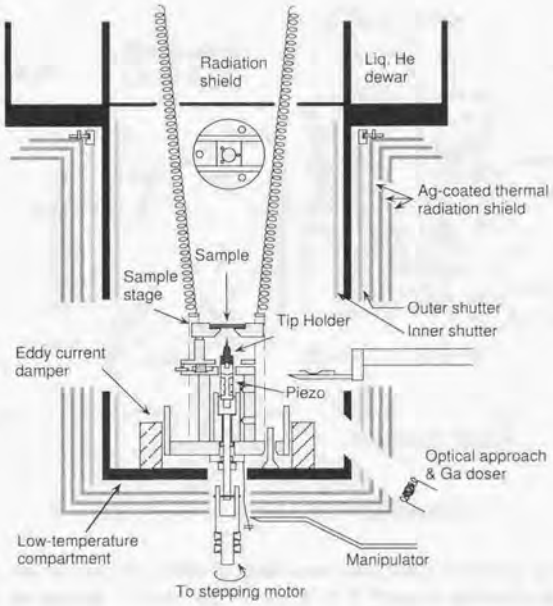

Figure 3.1: Schematics of the STM unit mounted inside the thermally shielded compartment.

3.1.2 STM unit

The STM unit contains a sample, coarse X-Y movement system, piezoelectric tube scanner, tip approaching system, and an STM tip. The STM unit is mounted inside a thermally shielded compartment directly attached to the liquid helium dewar. The schematics of the STM unit and thermal shields are shown in Fig. 3.1. The compartment and body of STM unit are made of copper coated with silver, and surrounded by three radiation shields. In order to gain thermal conductivity between a dewar and a compartment, indium sheets were inserted at the contact between them. The temperature of the compartment was same as the temperature of coolant.

Coarse approach of an STM tip is accomplished with the conventional stepping-motor approaching system. A sample, mounted on a tantalum

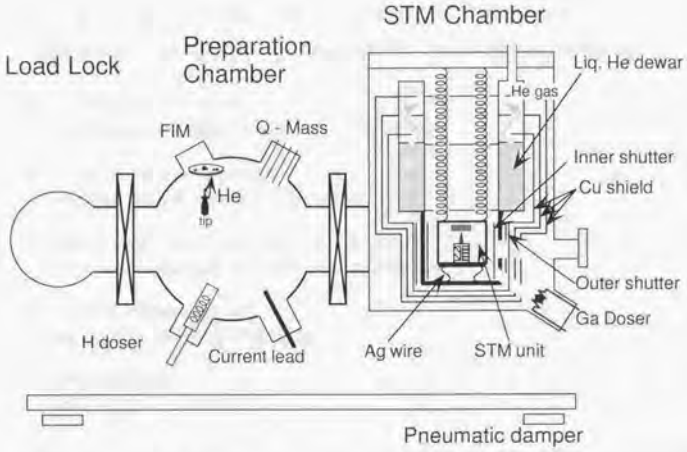

Figure 3.2: Schematics of the STM system.

holder, is put on top of the sample stage and rests on three metal balls simply by gravity. Coarse movement of X-Y stage is achieved by inertial sliding technique using shear piezoelectric devices, which enables the sample to move area of 4 mm×4 mm. This X-Y stage can be operated even at 30 K. The optical access to the sample and the STM tip is provided through the openings of the thermal radiation shield, compartment, and two radiation shield shutters.

3.1.3 UHV chamber

The UHV housing consists of three chambers isolated by gate valve: a load lock, a sample and STM tip preparation chamber, and a low-temperature STM chamber (Fig. 3.2). The base pressure of preparation chamber is in the 10^{-11} Torr range. The pressure of STM chamber is also in 10^{-11} Torr range when the dewar is at low temperature due to the cryopumping effect of the dewar. Preparation chamber and STM chamber are independently equipped with 120 ℓ/s ion pump and 1600 ℓ/s Ti sublimation pump.

The load lock, pumped by 250 ℓ/s turbo molecular pump, is used to exchange samples and STM tips in and out of the UHV environment. Four

stages are equipped for temporary sample and STM tip storage.

The preparation chamber is equipped with the following facilities.

1. Hydrogen atom doser:
   to prepare hydrogen-terminated Si surface.
2. Field ion microscope (FIM):
   to clean and shape an STM tip apex.
3. Quadruple mass spectrometer (Q-mass):
   for leak check and residual gas analysis.
4. Various-element doser:
   up to four different elements.
5. Current lead:
   for resistive heating.

Samples and STM tips are transferred by the horizontal linear-motion feedthrough in the UHV chamber. The characteristic feature of this STM system is that a sample and an STM tip can be changed to new ones easily. It only takes less than five minutes to change both the sample and the STM tip.

The STM chamber consists of dewar, STM unit, and thermal isolation shield. Also it is equipped with a Ga doser. Details are described in the following sections.

3.1.4 Vibration isolation

An STM observation on an atomic-scale resolution requires sophisticated vibration isolation system. Mechanical vibrations are isolated by mounting the whole STM system on a pneumatic vibration damper (Fig. 3.2). In UHV chamber, an STM unit is suspended by four springs to isolate vibrational noise. The springs are attached to the top of the STM chamber. The length of spring is about 90 cm, resulting in the cut off frequency of approximately a few Hz. Longer the stretch length of the spring, the resonace frequecy become low. Four magnets are installed on the bottom of inner compartment for eddy current damping (Fig. 3.1).

Cables from the control electronics and power lines for ion pumps to the UHV chamber are carefully treated to prevent the vibration transmission. All the cables are fixed to the heavy basement of pneumatic vibration damper.

Then, the cables are once fixed to the damper stage, and finally, connected to the UHV chamber. Removal of external cables and equipment connected to the UHV chamber minimizes both the vibrational and electronic noise transmitted to a tunnel junction. A preamplifier box is tightly bound to the STM chamber. This is quite important to reduce vibrational noise.

The above vibration isolation treatments ensure atomic resolution. No bubbling noise was observed even when the liquid nitrogen was used for a coolant. The z resolution of 0.001 nm was achived due to all the treatments.

3.1.5 Cryogenics

An STM unit is surrounded by 4.2 K compartment wall when a dewar is filled with liquid helium. Temperature of a sample is measured by a AuFe-Chromel thermocouple attached to a sample stage (Fig. 3.1), 2 cm apart from a sample. In every case, a sample was set on an STM unit for an overnight before the experiment. This ensures that the sample temperature is as same as the sample stage and the thermocouple. The temperature at the bottom of the STM unit is also monitored. Usually, there was 2 - 5 °C difference between the sample and the bottom of STM unit.

Three copper shields and a radiation shutter (outer shutter) surround the compartment. All the shields, thickness 1 mm, and the outer shutter are coated by silver with mechanical polishing in order to reduce emissivity. The amount of radiation depends on the surface of the materials. Smooth surface has low emissivity and result in a little radiation. Inside the compartment, an Au-coated copper shutter (inner shutter) is installed.

The cylindrical outer shutter has four large openings at the side for tip and sample exchange. Moreover, it has four small openings for optical access and deposition. The outer shutter allows an experimental flexibility by employing door mechanism, which can be used in three different positions:

1. Four openings are used for direct access to sample and STM tip.

   This position is used to exchange a sample and an STM tip.

2. All openings closed for minimum radiation.

   This position is used while scanning or in cooling process.

3. Deposition position.

   Three small openings are able to access the sample and the STM tip. One of the small openings is used for *in situ* deposition of atoms on Si

surface. Rest of the openings are used for optical access to the sample and the STM tip.

These positions can be altered by rotating the outer shutter using gear mechanism. Optical access allows us, with the help of an optical microscope, to achieve a well-controlled tip approach.

Once a sample and an STM tip are mounted to a STM unit, inner and outers shutters are closed to reduce a thermal radiation. Inner shutter is suspended by stainless wires and closed by moving the shutter down, touching bottom of the compartment, using vertical linear-motion feedthrough.

When an STM unit is in a cooling process, the STM unit is pulled down to make mechanical contact with the 4.2 K compartment wall in order to gain thermal conductance. When the STM unit is suspended by the springs, the STM unit has no direct contact to the compartment. This results in good mechanical vibration isolation but weak in thermal contact to a dewar. The thermal conductivity depends on the contact surface area and on the contact pressure. We used wobble-stick-like manipulator to pull down the disc connected to the STM unit using stainless wire. In this position, not only cooling is achieved but also used when changing a sample and an STM tip.

In order to prevent temperature rise due to the decrease of thermal conductivity when the STM unit is suspended, bundles of silver braided wires are installed (Fig. 3.1). Due to the high thermal conductivity of the silver wires, good thermal contact is expected. The 4 cm long, ϕ0.05 mm, total of about 64 silver wires are used for a single bundle. Total of four bundles were conected between the STM unit and the compartment. Since the silver wires transmit the vibration to the STM unit, the wire should be highly flexible. For this purpose, we chose a very thin wire. Those wires were not twisted to make bundles.

Liquid helium dewar is surrounded by three thermal shield. The silver-coated copper shields are connected to the top of the dewar. The evavorated helium gas flow long distance before going out from the STM chamber, in order to exchange heat efficiently with copper shields. Consequently, evaporation enthalpy is used to cool the copper shields, which minimize thermal conduction and radiation to liquid helium.

Any mechanical and electrical connection to the STM unit is designed to reduce heat conducting into the STM unit. Every electrical lead is thermally anchored to liquid helium temperature. Thus, every wire connected to the STM unit remove heat from STM unit. Cooling down to 30 K from 90 K can be achieved within approximately 6 hours. The liquid helium dewar has 13 ℓ

capacity, and keeps the STM head low temperature for more than 15 hours (helium consumption rate 0.86 ℓ/hour). Refilling the liquid helium dewar will enable us to do much longer experiments. When liquid nitrogen is used for a coolant, a sample can be kept at approximately 90 K for three days with one full fill.

Liquid nitrogen can be frozen (freezing point 63.14 K) by reducing a pressure using a rotary pump. In this case, the sample temperature became as low as 77 K. The temperature of the sample is controllable, by adjusting the shutter opening area. Thus, the desired temperature within plus minus 1 K is able to obtain under controlled manner.

3.1.6 STM control system

In STM, a feedback system is used to control a tip-sample spacing in order to maintain a constant tunneling current. As the tip is scanned across a surface, variations in a sample topography and electronic structure affect the tunneling. The control system must react to bring the tunneling current back to a desired value by adjusting a voltage to the z-piezo to keep constant current. This is called a feedback control. In our STM control system, almost all the functions are integrated to a single personal computer (PC). The PC does the digital feedback calculations. All the software which control the digital feedback system was written by Mr. Seiji Heike (Advanced Research Laboratory, Hitachi, Ltd.).

We used a fully digital STM control system to obtain the functionality. The software is modified for more precise manipulation of H and Ga atom. Digital feedback system has advantages in flexible control of STM tip by computer software. Furthermore, it simplifies the implementation of techniques such as atom and molecular manipulation.

The tunneling current amplitude is converted to voltage signal by preamplifier (Burr Brown, OPA111). The gain of the amplifier was set to 10^8 V/A. The analog voltage signal is converted to 16-bit digital signal by A/D (Analog-to-Digital) converter. The computer calculates the output z-piezo voltage, and transfer the results to high-voltage amplifier via D/A converter. The feedback is executed every 100 μs.

3.1.7 Specifications

Sample temperature	30 K - 300 K $\approx$ 90 K using liquid nitrogen $\approx$ 30 K using liquid helium (8 K with low resolution)
Lateral (x-y) resolution	0.001 nm
Horizontal (z) resolution	0.001 nm
Coarse x-y movement	4×4 mm
Scan range x/y/z	100 nm/100 nm/100 nm at 300 K 60 nm/60 nm/60 nm at 30 K
Initial cool down time from 90 K to 30 K	6 hours
Time between liquid helium refills	15 hours
Vacuum	in 10^{-12} Torr range at low temperature

3.1.8 Troubleshooting and further improvements

Our object was to develop high-resolution UHV-LT STM. In that point, we achieved our goal. However, there is much room to improve the performance of this STM. In this section, possible ways to improve the STM performances are discussed.

Achieve more low temperature

First, we discuss how to achieve further lower temperature. Our STM unit is exposed to room temperature through the hole (4.5 cm^2). This hole is used for stepping-motor STM-tip approaching system. The radiation from the room temperature through the hole is estimated to be 22.5 mW using Stefan-Boltzmann law of radiation (emissivity of 0.1 is assumed). The lowest sample temperature is 30 K at this moment, however if this hole is substituted to the compartment wall, we can expect much lower temperature. We expect the sample to be approximately 14 K in this case.

In order to eliminate the hole, the STM-tip approaching system must be improved. Since the inertial approaching system or 'louse' approaching system requires no mechanical approach from the room temperature, substitution to those system is the best solution. We are planning to substitute the stepping-motor approaching system to the inertial approaching system.

Reduce helium consumption rate

The cosumption rate of the helium depends on the amount of heat flowing into the dewar. The thermal conduction through the dewar wall (thickness 3.5 mm) from the top of flange turned out be very large from the estimation. Although the dewar is made of stainless (this material has low thermal conductivity), the thickness of the dewar is too thick. Considering the mechanical strength of the dewar, 2 mm-thick wall is the best solution.

Achieve better resolution

Installing the preamplifier on the STM unit may be a good solution to further reduce the noise level. Shorter the distance between the tunneling junction and the preamplifier, the less noise. Moreover, thermal noise would be reduced. In this case, the operational amplifier which works at low temperature is essential. The checkpoints concerning the preamplifier are summarized as follows.

1. Input voltage vs. output voltage must be linear at all the temperature range.
2. Large dynamic range (tunneling current ranges from 1 pA to 10 nA)
3. Package of operational amplifier must be resistant to thermal stress.
4. Choice of capacitor which operates at low temperature
5. Low bias current (Si MOSFET is suitable).
6. Materials of the package must be suitable for UHV.

Some of the amplifiers were tested, such as OP80, OP111, AD8532, and JNU001D. A 100 Hz sinusoidal input wave was inputted, but the output became unstable below 50 K in all the tested amplifiers. However, some preamplifiers which work at low temperature are reported [88].

Obtain temperature dependence of data

Substituting inertial-sliding approaching system for present approaching system enables us to obtain the temperature dependent data The present mechanical stepping-motor approaching system has a problem that this method has difficulty in following a fabricated structure when a z-direction thermal drift is apparent. In order to follow the strucure in wide range of temperature, inertial-sliding approaching system is the best solution.

3.1.9 Example of atom manipulation

Atom manipulation was carried out using specially developed software which allows the STM tip to move as the mouse is moved. Thus, lateral position of STM tip with respect to an STM image is arbitrarily controlled.

Fig. 3.3 shows the example of atom manipulation at 94 K. The adsorbate species is unknown in this case. The atom manipulation was accomplished after Ga deposition. Since a Ga atom is mobile in the trough between two adjacent dimer rows at this temperature (more details are described in section 4.4), we speculate that some other impurity atom is manipulated. The procedures are as follows:

1. An STM image of the adsorbate atom and surrounding hydrogen-terminated Si(100)2×1 surface were recorded.
2. The STM tip was addressed near the adsorbed atom using mouse control.
3. The parameters V_s and I_t are gradually increased to a set voltage and current (with the feedback loop on). In the present case, the set voltage was V_s = -3.8 V, I_t = 20 pA was successful. (For other atom manipulation, V_s = -4 V, I_t = 100 pA was successful.)
4. The STM tip is laterally displaced (0.5 nm/s) across the surface to desired position with the feedback on, by dragging the mouse over the image.
5. Both the V_s and I_t are slowly returned to the imaging parameter (V_s = -2.0 V, I_t = 20 pA). That is, the STM tip is moved perpendicular to the surface where the STM tip-adsorbate interaction is negligible.
6. An STM image of the same area was recorded again and compared to the first image to see the lateral movement of the atom.

Fig. 3.3(a) shows the initial position of the manipulated adsorbate atom. The adsorbate atom was first moved to the lower left along the dimer row (Fig. 3.3(b)). Then it was returned to original position (Fig. 3.3(c)). Some DBs are fabricated by applying a pulse of V_s = 2.9 V and I_t = 0.8 nA. (Fig. 3.3(d)). Next, the adsorbate atom was brought near the DBs (Fig. 3.3(e)). Note that the electronic charge distribution is altered due to the adsorbate. Finally the adsorbate atom is bonded to the DBs (Fig. 3.3(f)).

Due to the pronounced anisotropy of the surface, manipulation of the atom along the dimer row proceeds readily in the case shown in Fig. 3.3.

In this manipulation process, whether the STM tip is pushing or pulling the adsorbate atom was not able to be determined.

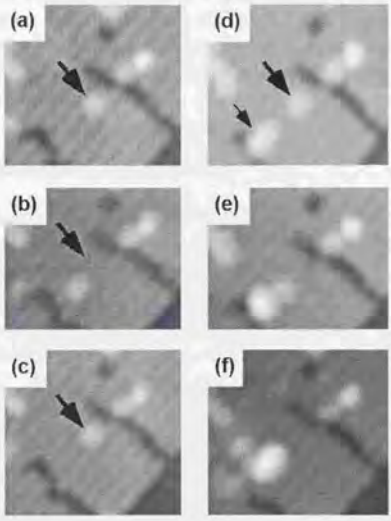

Figure 3.3: Examples of the atom manipulation at 94 K (9 nm× 8 nm, V_s = -2.0 V, I_t = 20 pA). (a) Initial position of the atom. The large arrow show this original position. (b) The atom is manipulated to the lower left. (c) The atom is returned to the original position. (d) Then, the DBs are fabricated (small arrow). (e) The atom is brought near the DBs. Note that the charge distribution of DBs are altered compared with (d). (f) The atom is finally bonded to the DBs.

3.2 Preparation of STM tips

A quality of an STM tip apex is a very important factor in STM experiments, since an STM image largely depends on the STM tip apex. Therefore, an important first step for the experiments is the preparation of a very sharp tungsten STM tip. However, *more important factor is the STM tip modification while in tunneling region.*

3.2.1 Electrochemical etching

There are many ways to prepare STM tips [89, 90]. In our experiments, ⟨111⟩ oriented single-crystal tungsten wire was sharpened by electrochemical etching [91] and used as an STM tip.

The procedure of tungsten-tip etching is very simple but requires a bit experience. The 0.25 mmϕ ⟨111⟩ oriented single-crystal tungsten wire was inserted 2 to 3 mm into solution. The solution was 25% NH_3OH, supersaturated with NaCl. The AC frequency of 50 Hz at the amplitude of 5 V_{RMS} resulted in satisfactory STM tips.

The tip was etched for about 5 to 10 seconds followed by the observation of the tip apex using an optical microscope. The etching was repeated until sufficiently sharp tip was obtained. If the observed tip apex was gradually disappearing (become transparent) at the magnification of $\times$1200, we regarded the tip to be enough sharp, and the tip was transferred into an UHV chamber. This determination of tip apex was where the experience was required. The same STM tip was used many times by re-etching the tip apex.

A concentration of NaCl plays crucial role in this etching process. A sharp tip can not be fabricated if the concentration is low. In order to increase the concentration, warming the solution to supersaturate NaCl was very effective.

The etching process leaves oxides on a tip apex. After transferred into an UHV chamber, the STM tip and a tip holder were outgassed with resistively heating the tantalum plate attached to the tip holder. Then, the contamination of the tip apex was removed and the tip apex was shaped using a field ion microscope (FIM) [92].

An FIM is an another apparatus which can image atoms and structures in real space. The observation of individual atoms on a surface was first reported by means of FIM. However, the surface must be very sharp, with a radius of at least a few hundred nanometer. The STM tip is placed facing an electrode (ground voltage), and a large positive voltage, usually up to

5 - 10 kV, is applied to the tip. Helium gas was introduced into preparation chamber for imaging gas, at the pressure of 5×10^{-5} Torr.

The interaction of an electric field with induced dipole moment in He atom draws the He atoms into a region of strongest field, that is, the step edge of a terrace. At a few Å from the tip, the electric field becomes so strong that the electron of the He atom transfer to the tip. When this happens, the He atom becomes positively charged ion, and is repelled from the tip toward the electrode. If the field strength is adjusted so that the ionization occurs only when the He atom comes very close to the surface, the angular distribution of ions from the tip would reflect the microscopic structure of the surface through the structure of the field in the immediate vicinity of the surface. The magnification ratio depends on the radius of the hemispherical sample.

A typical FIM image of a tungsten tip is shown in Fig. 3.4 (courtesy of Dr. Hashizume). Each bright spot corresponds to a tungsten atom of a terrace edge . With the increase of the applied voltage, oxides evaporate and a clean tungsten surface appears. Further increase of voltage induces field evaporation.

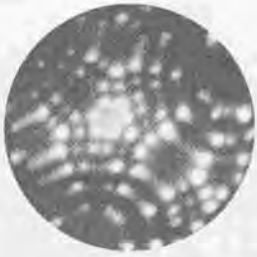

Figure 3.4: Typical example of FIM image of the tungsten tip. Each bright spot corresponds to a terrace edge atom. (Courtesy of Dr. T. Hashizume)

3.2.2 STM tip modification while tunneling

The most important step to obtain good data is the STM tip apex modification while tunneling. The atoms at the tip apex are very easy to move and become double and triple protrusions easily. These tips result in extraordinary STM image. The theoretical calculations on resolution of STM image reveal that the resolution is determined by the atomic structure of the tip

apex and that the atomic-size protrusion on the tip apex is essential for the atomic resolution [93]. To obtain high reproducibility and high-resolution STM image, it is quite important to re-shape the tip apex while in tunneling region.

It is well known that a high bias voltage or a large tunneling current applied to a tunneling junction can alter the atomic shape of the tip apex and/or the atomic arrangement of the sample surface [28]. The atomic arrangement of an STM tip apex was modified by increasing the tunneling current from 20 pA (imaging tunneling current) to typically 0.1 - 5 nA. In this condition, the sample bias voltage was slowly (10 V/s) increased from 2 V (imaging voltage) to 6 - 10 V, in either polarity. These tunneling current and bias voltage were kept for 3 - 5 seconds, and was slowly returned to imaging parameters.

This treatment changes the very local tip apex and results in high-resolution STM tip. Sometimes the STM tip become more dull, but in many cases the STM tip become better and recover atomic resolution. These controlled process was repeated until the tip apex becomes successful STM tip. *This technique indeed changes the quality of STM images, and consequently, the quality of the experiments.*

3.3 Sample preparation

A Si(100) sample (As-doped, n-type, 7 to 18 mΩ-cm) was cut from a commercial wafer into a $2 \times 14\,\mathrm{mm}^2$ rectangle and was set on a sample holder made of tantalum. After being transferred into an UHV sample preparation chamber, the sample was kept 650 °C overnight for outgassing. An atomically clean Si(100)2×1 surface was prepared by repeated resistive heating to 1260 °C at a pressure not exceeding 2×10^{-10} Torr. The temperature of resistively heated sample was measured with an infrared pyrometer, using an emissivity of 0.62 (empirical value).

Hydrogen termination was achieved by exposing the clean surface, kept at approximately 350 - 400 °C, to an atomic-hydrogen flux. Pressure as high as 2×10^{-8} Torr were kept for 10 min to saturate the surface. Below the range of a pyrometer (under 550 °C), temperatures were estimated by extrapolating a input-power vs. annealing-temperature curve ($P = aT + bT^4$, P: input power; a,b: constant; T: temperature) using the Stefan-Boltzmann law of radiation.

The atomic hydrogen atoms were obtained by decomposing hydrogen molecules with a resistively heated tungsten filament, which was set 5 cm away from the sample surface. A 0.15 mmϕ tungsten wire was wound like a coil as a filament and inserted into a tube made of Al_2O_3 ceramics. Hydrogen

molecule gas, introduced from leak valve, flow through the tungsten filament which was resistively heated to approximately 1500 °C. At this temperature, H_2 is fully dissociated and atomic hydrogen is produced [94].

Chapter 4

Results and discussion

This chapter focuses on the discussion of experimental results compared with the first-principles calculations. Progress in the following studies on a hydrogen-terminated Si(100)2×1 surface are discussed.

1. Hydrogen atom desorption using an STM tip.

   The methods of hydrogen atom desorption at room temperature and at low temperature (at approximately 35 K and 100 K) are presented.

2. Electronic structures of various DB structures.

   Various atomic-scale dangling-bond (DB) structures are fabricated and studied. For the DB structures made of only unpaired DBs, we observe charge redistribution in the DB structure. The DB structures made of only paired DBs show a semiconductive characteristics. The DB structures made of both the unpaired and paired DBs show finite DOS at E_F. Origins of these structural changes and their electronic structures are discussed.

3. Jahn-Teller distortion in DB structures.

   The atomic structures made of only unpaired DBs show interesting similarity in relaxation process with molecules, such as polyacetylene. Thus, we may call the structure as artificial pseudo-molecules. The interesting properties include Jahn-Teller distortion and soliton motion in the DB structures.

4. Adsorption potential energy surface imaging.

   Atomic-scale surface migration of Ga atoms are studied using STM and first-principles calculations. Gallium atom migrates in a 1D potential

well confined by adjacent dimer rows and local dihydride defects, and is observed as a continuous linear protrusion (Ga-bar structure) at a narrow range of temperature near 100 K. We point out that the height of the Ga-bar structure maps out a local adsorption free-energy variation. The possible effects of sub-surface impurity to the free-energy variation are discussed.

These topics are discussed based on the major questions presented in Chapter 1.

4.1 Hydrogen atom desorption

After the first demonstration of hydrogen atom desorption from a hydrogen-terminated Si(100)2×1 surface by Lyding *et al.* [40], several groups have successfully fabricated DB structures. At this stage in 1999, we are the only group who reports on the hydrogen atom desorption at the temperature range of 30-110 K.

4.1.1 At room temperature

A linear-chain of DBs (DB structure) on a hydrogen-terminated Si(100)2×1 surface was fabricated by applying a large bias voltage and a tunneling current. Two methods were used to desorb individual hydrogen atoms at room temperature. One method was to move an STM tip while applying a sample bias voltage of $V_s = +3.4\,\mathrm{V}$ and a tunneling current of $I_t = 1.3\,\mathrm{pA}$ at a rate of 1 nm/s [95]. These bias voltage and tunneling current resulted in the DB structures which were one- to two-dimers wide, however, these values depend on an STM tip apex. By applying larger bias voltage or tunneling current, wider structure could be fabricated.

The other method was to apply a pulse bias voltage and a tunneling current to the sample. An STM tip was first positioned above the selected atom, and then the pulse bias voltage and tunneling current were applied. The typical values were $V_s = +2.9\,\mathrm{V}$ and $I_t = 400\,\mathrm{pA}$. The pulse duration time ranged from 100 to 300 ms.

When the pulse voltage was larger than $V_s = +3.0\,\mathrm{V}$, extraction of only a single hydrogen atom became difficult, and wide-area extraction and/or impurity adsorption from an STM tip frequently occurred. When the pulse voltage was smaller than $V_s = +2.6\,\mathrm{V}$, hydrogen atom was hardly extracted.

In order to detect hydrogen atom desorption, an STM-tip height (z piezo-actuator voltage) and a tunneling current were monitored while the pulse was applied to a sample. The STM tip was retracted by approximately 0.4 nm during the voltage pulse, by a feedback system. The net difference of the STM-tip height before and after the pulse was approximately 0.1 nm, which corresponds to the height of an isolated unpaired DB. In this way we were able to accurately detect the hydrogen desorption without imaging, just by detecting the STM-tip-height position change. The reliability of tip displacement as an indicator of hydrogen desorption was quite high.

An uncontrollable transient current at the increasing and decreasing edges of the square-wave pulse induced the hydrogen atom desorption. The re-

sponse of the piezo actuator is much slower than the voltage change, and an overshoot current led to desorption of one or more hydrogen atoms for each pulse. The tunneling current showed an overshoot of more than 5 nA typically for 5 ms at the increasing edge when a voltage was abruptly changed. When the voltage increasing rate was slow, the overshoot current did not appear. In this case, the desorption did not occur.

Two distinct regimes for hydrogen desorption were observed and the mechanisms were proposed by Shen *et al.* [96]. According to their experiments, above electron energies of about 6 eV ($V_s > 6\,\mathrm{eV}$), a desorption yield is energy independent, and has been attributed to the direct electronic excitation of the Si-H σ bonding to anti-bonding transition. Below 6 eV ($V_s < 6\,\mathrm{eV}$) the desorption yield for hydrogen decreases by several orders of magnitude, compared to above 6 eV. In this region, the yield is highly dependent on both electron energy and current density. Desorption in this regime is explained by a multiple vibrational heating mechanism [97].

Lyding *et al.* reported that the hydrogen atoms were only desorbed when a sample is biased positive [40]. However, Huang *et al.* [98], Thirstrup *et al.* [99], and our experiments show that the hydrogen atoms can be desorbed even at negative sample bias voltage. In our case, larger voltage and current were required to desorb at the negative sample bias voltage than at the positive sample bias voltage. Huang *et al.* speculate that this desorption process may have a electronic-field-induced mechanism [98]. Recently Stokbro *et al.* reported that the desorption is caused by vibrational heating of the hydrogen atom [99].

The fabricated structure was sometimes altered by the flipping of H atom to adjacent Si atom in a same Si dimer (intradimer hopping [100]) or hydrogen atom adsorption. The intradimer hopping barrier of hydrogen atom is experimentally observed as 1.0 ± 0.2 eV, and hopping across dimer is observed as more than 2.0 eV [101]. The theoretical calculations using local density functional approach predicts 1.2 eV for intradimer hopping and 1.8 eV for across the dimer row [102], which are in good agreement with the experiment. These values are sufficiently larger than the thermal energy at room temperature (25 meV). Consequently, the stability of the DB structure is very high.

4.1.2 At low temperature

Figure 4.1 shows the filled-state STM image of DB structures fabricated at 107 K. The lines used to make each character are a few nanometers wide.

An STM tip was placed on top of the desired hydrogen atom, and moved

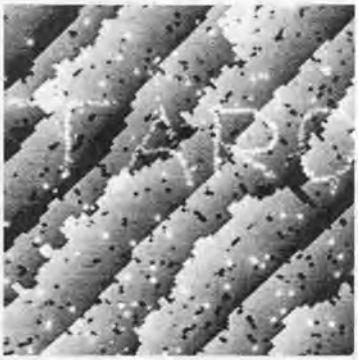

Figure 4.1: An STM image of fabricated DB structure on hydrogen-terminated Si(100)2×1 surface. The character "TARO" (the author's name) was fabricated and observed at 107 K. Each line consisting the character is a few nanometers wide. (75 nm × 75 nm, V_s = -2.0 V, I_t = 20 pA)

parallel to the dimer row. A feedback system was turned off during the tip movement in order to keep a constant tip-sample distance. This procedure keeps the interaction between the STM tip and the hydrogen atom constant. The STM tip height was maintained constant by measuring the sample gradient just before the manipulation. We routinely obtained DB structures one- to two-dimers wide (0.8 to 1.6 nm) by moving the STM tip at a speed of about 1 nm/s while applying $V_s = +2.8$ V and $I_t = 0.9$ nA. In this way, we could fabricate arbitrary DB structures on the hydrogen-terminated Si(100)2×1 surface. At 40 K, $V_s = +2.7$ V and $I_t = 0.7$ nA resulted in one- to two-dimer-wide DB structures.

We found that the required tunneling current and sample bias voltage to desorb hydrogen atoms at low temperature was much lower than the required current and voltage at room temperature. At almost same time, Foley *et al.* reported that a hydrogen atom is a factor of about 300 easier to desorb at 11 K than at 300 K [103]. Our group also noticed this result but we did not perform quantitative study. Their group explained this large temperature dependence by a model that takes into account the increase of a Si-H vibrational lifetime at low temperature [103].

4.2 Electronic structure and relaxation of DB structure

All the DB structures on a hydrogen-terminated Si(100)2×1 surface consist of paired and/or unpaired DBs (Fig. 2.5). Three different types of DB structures were fabricated: DB structures made of only paired DBs, DB structures made of only unpaired DBs, and a mixture of both paired and unpaired DBs. The electronic structures of DB structures are discussed base on the first-principles calculations by Watanabe *et al.* [51]. The experiments were performed both at room temperature and at low temperature (near 100 K). All the experimental data presented in this dissertation were obtained using the constant-current imaging mode.

4.2.1 DB structure made of only paired DBs

First, the electronic structure and relaxation of an artificial DB structure made of *only paired DBs* are discussed. Figure 4.2(a) shows the DB structure fabricated at 110 K. Dimers in this DB structure are buckled and the structure is observed as a zigzag line similar to the asymmetrical buckled dimers observed in Si(100) $p(2\times2)$ or $c(4\times2)$ reconstructions (Fig. 4.2(b)). It is reasonable to conclude that the DB structure is made of only paired DBs, because of this buckling feature and also because the DB structure is located at the center of a dimer row. More evident way to prove this is to observe empty state. The Si dimers should be observed as symmetrical in this case.

This buckling feature was even observed at room temperature. At this temperature, the buckled dimers are only stabilized near the defects or an adsorbate atom on a clean Si(100)2×1 surface [71]. In the present case, the buckling is stabilized either by the 1D characteristics of the structure (Peierls distortion [104]) or by the edge effects (both edges of the structure are somewhat disordered by the adjacent hydrogen-terminated Si dimers and may stabilize the buckling). A paired DB, whose adjacent dimer in a same dimer row is hydrogen-terminated, appears as symmetric in STM image (Fig. 2.5(c)). This result implies that the buckled dimer is flipping rapidly between two degenerate states. The calculation suggest the buckling in this configuration [105] and support this flipping. However, if the unpaired DB is in a array, such as in Fig. 4.2(a), the flipping is suppressed and buckling direction alternates in a same dimer row. This result suggest that 1D structure plays important role in the pinning of the buckled dimer.

On the theoretical side, buckling in the DB structure is predicted by the

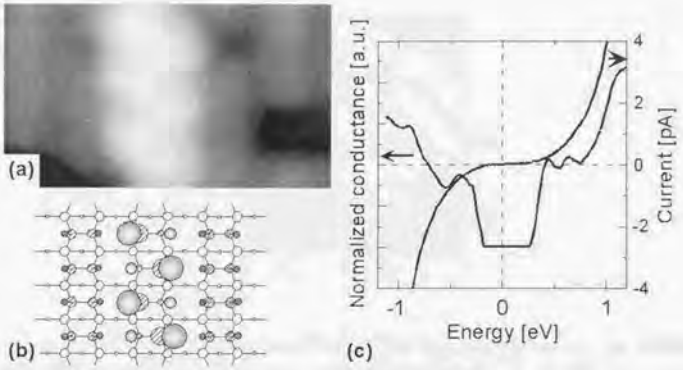

Figure 4.2: (a) Filled-state STM image of DB structure made of only paired DBs at 110 K (2.6 nm × 3.8 nm, V_s = -2.0 V, I_t = 100 pA). The buckling feature is observed. (b) Schematics of a buckled DB structure. (c) Normalized conductance curves and current-voltage (I_t-V_s) characteristics obtained on the DB structure made of only paired DBs. The tunneling junction is stabilized at V_s = -2.0 V and I_t = 100 pA.

first-principles calculations [51, 53]. Figure 4.3 shows the calculated band structure of the infinite-length DB structure made of only paired DBs by Watanabe *et al* [51]. Details of their calculation methods are described in section 2.4. The calculation predicts the direct energy gap of 0.49 eV and indirect energy gap of 0.35 eV.

The tunneling spectra in Fig. 4.2(c), obtained from another DB structure made of only paired DBs, have an energy gap of approximately 0.5 eV. We speculate that the peaks just below and above the enegy gap originate from π bonding and π^* antibonding states caused by the interaction between DBs of Si atoms on a dimer. The mechanism of the energy gap formation is similar to that of the band gap observed on the clean Si(100)2×1 surface.

This DB structure is expected to have an 1D character, according to the calculations by Haye *et al.* [53]. Compared with the clean Si(100)2×1 surface, the calculation predicts that the hydrogen passivated dimer row reduces the dispersion of the surface bands in the direction perpendicular to the dimer rows. This dispersion is 0.02 eV, as compared to 0.15 eV on the clean surface. Consequently, even when the DB wires are separated by only one hydrogen-terminated row, the surface states of the DB structure have a

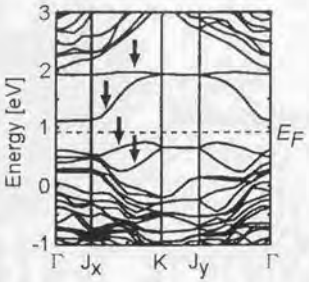

Figure 4.3: Calculated band structure of DB structure made of only paired DB. The arrows show the surface-state band generated by the DB structure. Note the larger dispersion in the direction along the DB structure (J_x to K, and J_y to Γ). The 4×2 unit cell is used. The unit cell and the surface Brillouin zone is shown in Fig. 2.8.

clear 1D character.

4.2.2 DB structure made of only unpaired DBs

A question arises, what will happen if a DB structure is made of *only unpaired DBs*? Fig. 4.4(a) shows the gray-scale filled-state STM image (three-dimensional view) of the DB structure fabricated at 96 K. A row of hydrogen atoms was extracted along the Si dimer row parallel to the dimer-row direction (schematically shown in Fig. 4.4(b)) and the DBs are imaged off-centered on the dimer row.

The fabricated DB structure showed striking difference from the ideal structure illustrated in Fig. 4.4(b). That is, we found that DBs are seen only alternately, as schematically shown in Fig. 4.4(c). The DB structure in Fig. 4.4(a) has eight protrusions in a row, however, it is fifteen dimers long. The distance between the peaks is approximately 0.77 nm, which implies that DBs are observed alternately. The 2×1 unit cell is doubled and a new 2×2 unit cell is formed. We could not observe any protrusions between the distinct alternate peaks, even when the Si dimers are clearly observed. We also observed alternating DBs at room temperature.

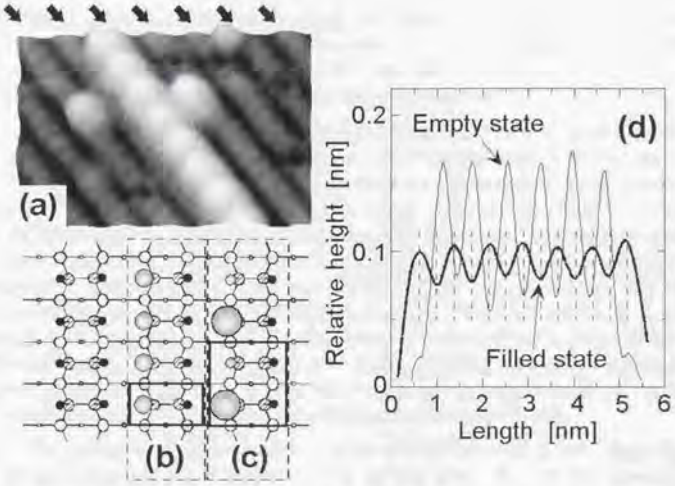

Figure 4.4: (a) A low-temperature (96 K) STM image (gray-scale three-dimensional view) of a dangling-bond (DB) structure fabricated on the hydrogen-terminated Si(100)2×1-H monohydride surface (7 nm × 4 nm). The black arrows show the center of the Si dimer rows. (b),(c) Schematic views of DB structures on the Si(100)2×1 monohydride surface. Blank circles denote Si atoms and filled circles denote hydrogen atoms. Half-tone circles denote DBs, where the size reflects apparent height observed by STM. A DB structure made of unpaired DBs before and after relaxation is shown in (b) and (c), respectively. The 2×1 and the new 2×2 unit cells are shown by the black box. (e) Cross-sectional views of a thirteen-DB structure observed at V_s = -2.0 V (filled state) and +2.0 V (empty state). Both data was obtained at V_s = -2.0 V, I_t = 20 pA.

We observed peak shifts of DBs in the same structure between the empty- (V_s = -2.0 V) and filled- (V_s = +2.0 V) state STM image. Figure 4.4(d) shows a cross-sectional views of a thirteen-DB structure (defined as a DB linear-chain structure made of thirteen unpaired DBs) fabricated at 100 K. The dark valleys in the filled-state image become bright protrusions in the empty-state image. The DBs were also imaged bright alternately in the empty-state STM image. This is different from the buckled structure because empty-state STM image of buckled dimers show symmetrical dimers, which would give equivalent height in cross sectional view. The spatial shift of the peaks between

the filled- and the empty-states reveals that unpaired DBs does exist in the valleys between the peaks in the filled-state image. Considering these STM results, we conclude that a change in electronic structure, accompanying charge redistribution, has occurred in this DB structure.

The structural relaxation of the infinite-length DB structures can be explained in terms of the recent first-principles calculations by Watanabe *et al.* [51]. Each Si atom in DB structure has one DB and each bond is occupied by a single electron, before the relaxation. A row of such bonds forms a half-filled band on the surface within the bulk band gap. This surface-state band is half-filled when Peierls distortion [104] is not taken into account. However, this distortion opens up a direct energy gap of 0.125 eV and an indirect energy gap of 0.025 eV (Fig 4.5(a)). A Peierls distortion is a periodic symmetry-lowering lattice distortion accompanied by a redistributed periodic charge called charge density waves (CDW). This phenomenon is most commonly observed in crystals of reduced symmetry, such as quasi-two-dimensional [106] or quasi-one-dimensional materials [107].

The direction of this distortion of first-layer Si atom is not along the DB structure but perpendicular to the surface (Fig. 4.5(c)). In first-layer Si atom, a height difference of 0.016 nm arises between the neighboring Si atoms in the DB structure. These height modulation is induced by the lateral displacement of the second-layer Si atoms. The calculated lateral displacement was 0.002 nm. The second-layer Si atoms are displaced toward the right or left alternately and they tend to pair up, resulting in a 2×2 unit cell.

From this distortion, energies of the DBs and charge distribution vary, so that certain DBs can be seen at some bias voltages but not at others. Figures 4.5(d) and (e) show the contour plots of calculated wavefunction intensity distribution (log scale), 0.1 Åabove the hydrogen atom. Although, this is too close to the surface compared to a STM tip-sample spacing (approximately 1nm), they clearly show 2×2 symmetry.

These STM observations and theoretical calculations lead us to conclude that a charge redistribution and a possible lattice distortion are taking place in these DB structures, and hence result in the alternate topographic peaks. A relatively long DB structure such as the one in Fig. 4.4(a), can be modeled by a periodic unit structure if the effect of edges is negligible. The distortion in the middle part of the DB is well described by the instability in 1D metal resulting in Peierls distortion.

First-principles calculations for the infinite-length structure predict the energy gain of 14 meV per 4×2 unit cell, which corresponds to the temperature of 160 K. Consequently, this phenomenon is only expected at low

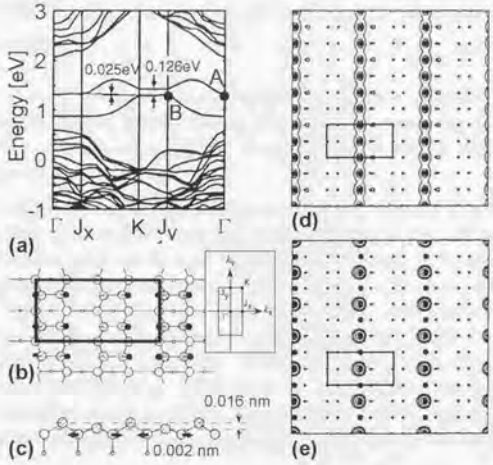

Figure 4.5: (a) Calculated band structure of DB structure made of infinite unpaired DBs. The structure is parallel to the dimer row. Along the DB structure (J_x to K, and Γ to J_y), the band has larger dispersion compaired to perpendicular to the structure. (b) The box shows the schematics of 4×2 unit cell used in the calculation. The inset shows the surface Brillouin zone (c) A cross-sectional view of the calculated distortion of the infinite-length DB structure. (c) and (d) are contour plots of wavefunction intensity calculated at wave-vector at A and B in (a), respectively. The boxes show the unit cell shown in (b). (Courtesy of Prof. S. Watanabe.)

temperature. In contrast to these calculations, we observed this phenomena even at room temperature. It is known that the energy gap calculated using local density functional approximation tend to result in smaller energy gap than experiment. Furthermore, the first-principles calculations by Watanabe *et al.* deal with infinite-length DB structures and do not fully appreciate finite-length and electron correlation effects. Considering these, we speculate that the energy gap of the DB structure is more than 25 meV.

4.2.3 DB structure made of both paired and unpaired DBs

The above discussions imply that the periodic structure either made of only unpaired or only paired DBs is always stabilized and an energy gap will open up. Therefore, random arrangement of unpaired and paired DBs may result in the suppression of stabilization.

Figure 4.6(a) shows the DB structure which is a mixture of both unpaired and paired DBs (mixed structure), parallel to the dimer row, as well as a couple of DBs in the next dimer row. Figure 4.6(b) shows I_t-V_s characteristics and normalized conductance curves $((\mathrm{d}I_t/\mathrm{d}V_s)/(I_t/V_s))$ obtained on the DB structure. This DB structure has finite DOS at E_F, whereas no DOS is observed for the hydrogen-terminated dimer at E_F (Fig 2.7(a)). Characteristic peaks at energies of -1.7, -0.8 and +0.8 eV relative to E_F are observed in the normalized conductance. Similar results are obtained for the tunneling spectra at different positions of the DB structure in Fig. 4.6(a) and also for the DB structures fabricated perpendicular to the dimer row [95].

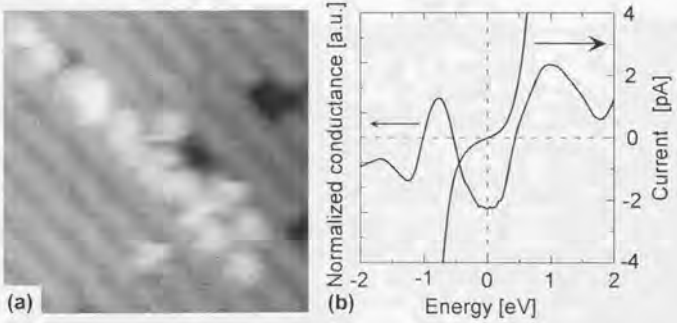

Figure 4.6: (a) Filled-state STM image of a DB wire parallel to a dimer-row direction (9 nm×9 nm, V_s = -2.0 V, I_t = 100 pA) and (b) I_t-$V_s$characteristics and a normalized conductance curve recorded on the DB structure.

In section 2.3, we described that an isolated unpaired DB shows an finite DOS at E_F. Therefore, possible origin of the DOS near the E_F is from the unpaired DBs in the DB structure. We speculate that two distinct peaks at -0.8 and +0.8 eV (observed in the normalized conductance curve in Fig. 5(a)) represent the bonding and antibonding band resulting from the DB

structures made of DB pairs.

We believe that the stabilization does not occur if the unpaired and paired DBs are suitably mixed. Consequently, the DB structures show finite DOS at the E_F. The best configuration which gives the maximum DOS is not clear. However, this experiment suggests that the mixture result in doping effect and avoid stabilization. When the structure is mainly made of unpaired DBs, the paired DB act as dopant. These result implies that the characteristics of stabilized structure can be altered by adding dopant atoms. There is many experiments to do for this mixed structure.

4.2.4 Discussion

It is interesting to note that the electronic structure reflects the subtle difference in atomic-scale DB configurations. We discussed the electronic structure depending on the width of the DB structure. The STM/STS results enable us to distinguish the changes in electronic structures depending on the DB configurations. Table 4.1 summarizes the experimental and theoretical results.

	Experiment (STM/STS)	Predictions of first-principles calculations [51]
(a) only paired DB	Buckling features. Energy gap (E_g) =0.5 eV.	Buckling features and semiconductive band structure. E_g=0.5 eV.
(b) only unpaired DB	Relaxation and charge redistributions. DBs are observed alternately.	Peierls distortion. DBs should be observed alternately. E_g=0.025 eV
(c) paired and unpaired DBs are mixed (mixed structure)	DOS at E_F	No calculation available

Table 4.1: Summary of the results.

The relaxation occured in periodic structures such as DB structure made of only paired DBs and made of only unpaired DBs. The mixed structure is the most interesting structure due to its various combinations of paired and unpaired DBs. The effect of mixture should be carefully considered.

Haye *et al.* reported on the band structure of the $p(4\times2)$ unit cell with

one Na atom per Si dimer, adsorbed on DB structure made of only paired DBs [53]. The surface bands resemble those of the clean DB structure, however, the surface states resulting from the DB structure was half filled after Na adsorption. This structure is expected to have metallic properties. They have not yet done the calculation on larger unit cell [108]. The Peierls distortion may appear in this case. Hashizume *et al.*, indeed, deposited Ga atoms and formed Ga atom wire using DB structure [41]. Whether the Ga atom wire is conductive or not is very interesting.

We now discuss the transport in this DB structure. In one dimension, special aspects of physics will be involved. First the energy stabilization such as Peierls transition can not be prevented. The structure will end up with a gap in the band structure, which is insulating or semiconducting.

In pure 1D system, any disorder, whatever its magnitude, will induce localization at temperature $T = 0\,\mathrm{K}$ (the Anderson localization [109]). In other words, instead of being delocalized over the entire chain, the wavefunctions are limited to a given localization length λ. Thus, as soon as the chain length is larger than the localization length, charge carriers are not able to cross along the chain, that is, the chain is an insulator at $T = 0\,\mathrm{K}$. For $T > 0$, phonons are excited, which will have two opposite effects [110]: (1) being assisted by phonons, charge carriers can now move along by hopping. (2) scattering against the same phonons also restrains the motion of the charge carriers. Considering these, the atomic wire should be shorter than the localization length. A ballistic conduction is required to be used as conducting wire.

If the effect of electron correlation is not negligible in this system, another explanation for the I_t-V_s curve of mixed structure is possible. The effects of electron correlation and spin are known to cause purely 1D systems with a half-filled energy band to be always insulating within the constraints of the 1D Hubbard model. The DB structure made of both paired and unpaired DBs can be interpreted as carrier-doped DB structures. If the structure is made of only unpaired DBs, it may have a band gap in the tunneling spectra because one electron per site is just the same as a half-filled Hubbard model. This model predicts the so-called Mott-Hubbard insulator when the system is half filled and electron correlation is taken into account. Here, a DB pair plays the role of a carrier dopant or perturbation. Because of the localized π-bond in DB pairs, the electrons of unpaired DBs have some perturbation from the paired DB site, resulting in the carrier dope effect. The carrier-doped Mott insulator behaves as a metal, which may be the case in these DB structures. In this scenario, the finite DOS at the E_F is explained by the carrier-doped Hubbard model.

The naming of the distortion is old but new problem. It is quite ambiguous that how many atoms are needed to say Peierls distortion. If there is no edge effect, we may say it is Peierls distortion. If there are edge effect, we may say it is Jahn-Teller distortion.

Finally, we briefly comment on a possible peculiar electronic structure in the DB structure. In the case of a mesoscopic GaAs quantum wire [111], the temperature dependence of the conductance is well described by the finite-length Tomonaga-Luttinger Liquid. In a 1D structure, the effect of electron correlation is relatively strong compared with that in higher-dimensional structures. This implies that in an atomic-scale DB structure, more 1D like characteristic features can be observed and a Tomonaga-Luttinger Liquid may be achieved. In order to study this effect, temperature dependent STS must be studied.

4.2.5 Summary

The main results presented in this section are:

1. *The electronic structures vary depending on the width of atomic structure.*
2. The periodic structure either made of only unpaired or only paired DBs is always stabilized and an energy gap will open up.
3. The mixture of unpaired and paired DBs results in the doping effect and suppresses stabilization.

I conclude this section as follows.

"The periodic structure want to be semiconductive. In order to fabricate conducting atomic-scale structures, some perturbation such as doping should be introduced."

4.3 Jahn-Teller distortion in DB structures

Total-energy lowering in pseudo-one-dimensional structures by charge redistribution is one of the exciting topics in solid-state physics. The Jahn-Teller distortion [112] in a finite-length molecular system and the Peierls instability [104] in 1D metal system are two typical examples. It is known that soliton motion [113] decreases the energy barrier of structural change in the polyacetylene.

Linear-chains of DBs on a hydrogen-terminated Si(100)2×1 surface are fabricated and studied by using STM. Length-dependent charge redistribution was observed and first-principles calculations reveal that the second-layer Si atoms are displaced alternately to form pairs, which results in the Jahn-Teller distortion. In a short even-numbered DB structures, a lone second-layer Si atom which is not forming a pair exist and behave like a soliton, resulting in flip-flop motion of the charge in the first-layer DBs. The phenomenon is in analogy to a soliton motion in a polyacetylene. We point out that the odd-even problem, the edge effect, and the finite length of the DB structures must be taken into account in order to explain the experimental observations [114].

The experiments are performed at low temperatures (96 to 110 K) achieved by liquid nitrogen and a temperature-control shutter attached to a radiation shield. The STM images and cross-sectional views are obtained at V_s = -2.0 (filled state) or +2.0 V (empty state) and at a constant tunneling current of I_t = 20 pA.

4.3.1 Length-dependent distortion

In order to investigate the charge redistribution in short DB structures, we carefully fabricated two-, three-, four-, and five-DB structures (defined as a DB linear-chain structure made of five unpaired DBs along a dimer row). Figures 4.7(a) through (d) show gray-scale filled-state STM images of two-, three-, four-, and five-DB structures. Cross-sectional views of filled-state STM images for two-, three-, four- and five-DB structures are shown in Fig. 4.8. The apparent modulations observed in the height of the DB structures reflect the redistributions of the charge.

From the filled-state STM image of two-DB structure, the height difference between the two DBs is within an experimental error. There is a distinct node between two DBs, which is seen as a dark line perpendicular to the dimer rows in the STM image (Fig. 4.7(a)). No node was observed in the empty-state image (V_s = +2.0 V), and it was seen as one protrusion.

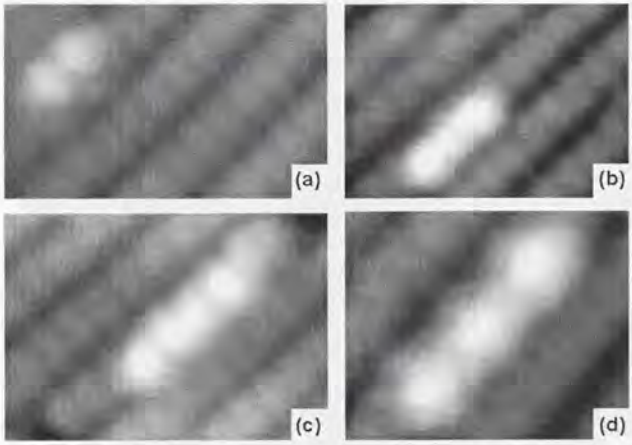

Figure 4.7: Filled-state STM images of (a) two-, (b) three-, (c) four-, and (d) five-DB structures [114]
(V_s =-2.0, I_t = 20 pA).

Apparent height changes of DBs are observed for the longer DB structures. The three-DB structure, seen as three protrusions, is located at lower right side of a dimer row in Fig. 4.7(b). In this case, the center DB is seen lower than both edge DBs. Interesting results are obtained for the four-DB structure (Fig. 4.7(c)). The DBs located at both ends are seen higher in filled state image, as usual, but the center two DBs are seen like 'buckled,' and the spatial symmetry is broken.

In the case of the five-DB structure (Fig. 4.7(d)), the distinct peaks are seen alternately, similar to the results described in section 4.2.2. We could not observe any protrusion between the distinct peaks, even if Si dimers are clearly observed. Furthermore, the spatial shift of peaks between empty and filled states are observed. Same characteristics were observed for DB structures made of seven, nine, and eleven DBs. The edge DBs are always seen as protrusions in all these DB structures.

These modulations cannot be explained by the calculations such as those carried out by Watanabe *et al.* [51], in which an infinite-length DB structure is assumed using periodic boundary condition. In order to reveal the origin

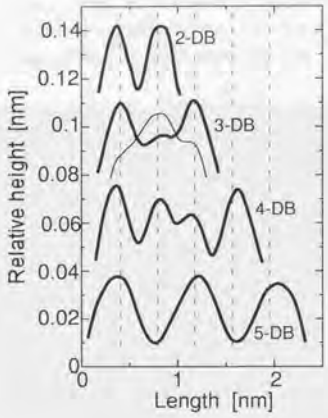

Figure 4.8: Cross-sectional views obtained from the filled-state images of two-, three-, four- and five-DB structures. A cross-sectional view of the empty-state image for the three-DB structure is also shown by a thin line in (d). The curves are arbitrarily offset vertically.

of this charge redistribution, Li *et al.* performed first-principles calculations dealing a large unit cell (4×8, two dimer rows with eight dimers each) based on a local density functional approach. The details of the calculation methods are published elsewhere [115, 116], and also described in section 2.4.

4.3.2 Odd-numbered DB structures

In the case of the DB structures composed of odd-numbered DBs (three- and five-DB structures), distinct alternate peaks are observed in the filled-state STM images and the edge DBs are always observed as protrusions (Figs. 4.7(b) and (d)). In three-DB structure, the height difference between the edge DB and the center DB is approximately 0.015 nm (Fig. 4.8). In an empty-state STM image of the three-DB structure, the center DB appeared to be 0.01 nm higher than the edge DBs (thin line in Fig. 4.8).

The first-principles calculation of the three-DB structure showed a remarkable qualitative agreement with the STM images. Figures 4.9(a) shows the contour map of the calculated filled DOS (2.0 eV below the Fermi energy) of the three-DB structure. Close ups for filled (V_s = -2.0 eV) and empty states

($V_s = +2.0$ eV) are shown in Fig. 4.9(b) and (c), respectively. Almost a unity charge of the center DB has transferred to the edge DBs. In contrast, the center DB has much higher empty DOS than the edge DBs.

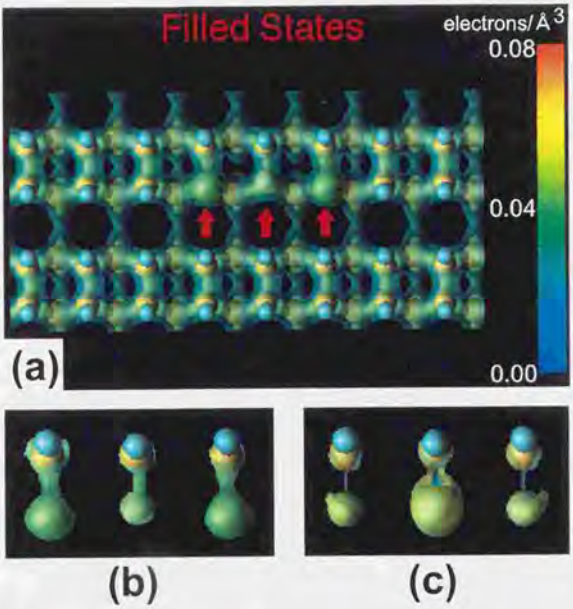

Figure 4.9: (a) A calculated contour map of the filled-state (2.0 eV below the Fermi energy) local density of states for a three-DB structure (Courtesy of Li *et al.* [114]). Yellow and blue spheres stand for Si and H atoms, respectively. Dimer rows are running horizontally. Red arrows indicate the position of DBs. Close up views of filled ($V_s = -2.0$ eV) and empty ($V_s = +2.0$ eV) density of states are shown for the three-DB structure in (b) and (c), respectively.

A vertical displacement of the first-layer Si atoms is accompanied by a lateral relaxation in the second-layer Si atoms resulting in the pair formation (Fig. 4.10(a)). When the second-layer Si atoms pair up, the backbond angle (schematically shown in Fig. 4.10(a)) becomes smaller, which lowers the DB energy [66]. More details are described in section 2.1. The numerical calcu-

lations suggest that the DB character of the center Si atom becomes more $p-like$ because the backbonds of the Si atom become more sp^2-like (backbond angle becomes larger due to the second-layer Si-atom displacement). In contrast, DBs of the edge Si atoms become more $s-like$ because the backbonds of the Si atoms become p^3-like. Since the $s-like$ orbital (the energy of this orbital is defined as E_{s-like}) is energetically more favorable than the $p-like$ orbital (the energy of this orbital is defined as E_p-like), a charge transfer from the center DB to edge DBs.

The calculated energy levels at the Γ point of wave-vector space showed that the energy levels corresponding to the DBs are stabilized by an opened up energy gap of 0.38 eV (Fig. 4.10(a) inset). The present numerical calculations assume a periodic arrangement of the DB structure. However, the 4×8 cell is large enough for us to regard the calculated DB structure as an isolated three-DB structure. These scenarios on the relaxation of the three-DB structure can be well described by a Jahn-Teller distortion in an artificial pseudo-molecule composed of three DBs.

The ideal three-DB structure contribute one electron per surface Si atom to a half-filled DB surface state. However, an energetically equivalent arrangement would place electrons on some sites and leave others empty. According to Jahn and Teller [112, 117], this type of electronically degenerate situation is unstable with respect to lattice distortions and lower the symmetry in order to remove the degeneracy. Generally, the distortions tend to lower the energy of occupied states and raise the energy of unoccupied states. This action opens up energy gap and clearly lowers the enegy of the entire system.

Pairing of the second layer Si atoms are common in all the odd-numbered DB structures, as is shown in Fig. 4.10(b) for the case of the five-DB structure. All the second-layer Si atom form pairs. We were able to interpret the STM images of seven- and nine-DB structures in a similar way. In all the odd-numbered DB structures, we predict that the edge DBs will always be observed as peaks and inner DBs will always be observed as alternate peaks.

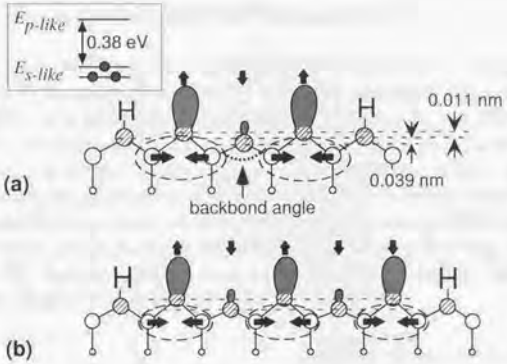

Figure 4.10: (a) A ball-stick model of the three-DB structure showing displacement patterns of the first- and second-layer Si atoms indicated by the arrows. The hatched and blank circles denote the first- and second-layer Si atoms, respectively. The amount of charge in the DBs is schematically expressed by the shaded ovals. The dotted oval shows the paired second-layer Si atoms. Dashed horizontal lines show the center of up and down Si atoms with DBs relative to the unrelaxed Si atoms. The calculated results indicate that the central Si atom with the DB moves downwards by 0.039 nm (toward the bulk) and the edge Si atoms with the DBs move upwards by 0.011 nm (toward the vacuum). The second-layer Si atoms are displaced 0.0016 nm laterally to form pairs. The inset shows the energy level diagram at the Γ point in wave-vector space associated with the three-DB structure. Filled circles stand for electrons. (b) A ball-stick model of the five-DB structure showing displacement patterns of the first- and second-layer Si atoms shown by the arrows. The second-layer Si atoms are displaced towards the right or left alternately forming Si pairs.

4.3.3 Even-numbered DB structures

Interesting results for the even-numbered DB structures are obtained. In the filled-state STM image of the two-DB structure, the height difference between the two DBs was within the experimental error, that is, less than 0.001 nm (Fig. 4.8). However, the calculated result for the two-DB structure suggests an inequivalent atomic height, resulting in inequivalent charge distribution. There are two degenate most-stable configurations in mirror symmetry, with a calculated flip-flop barrier of 48 meV, which is the energy difference between the relaxed structure and the structure with no distortion (Fig. 4.11(a)). A frequent flip motion, induced even at 100 K (Fig. 4.11(b)), results in the equivalent height of DBs observed in the STM image.

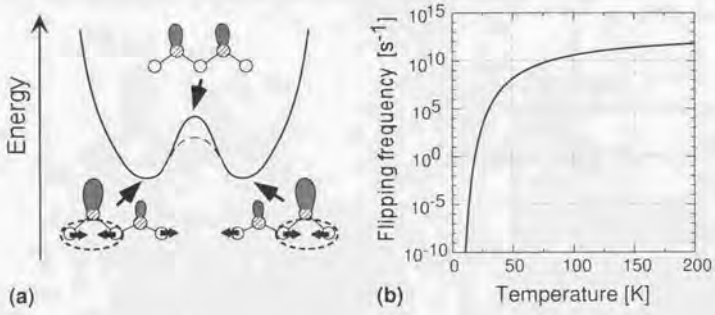

Figure 4.11: (a)Schematics of energy diagram. There are two equivalent most-stable configurations in mirror symmetry, with a calculated flip-flop barrier of 48 meV, which is the energy difference between the relaxed structure and the structure with no relaxation. (b) The estimated flipping frequency as a function of temperature. A frequent flip motion is induced even at 100 K and results in the equivalent height of DBs observed in the STM image.

The flip-flop frequency typically depend exponentially on temperature. We can estimate the flip-flop frequency f using a simple Arrhenius equation, $f = \nu \exp(-Q/kT)$, where ν is a pre-exponential factor, Q is an activation barrier, k is a Bolzmann constant, and T is a temperature. The pre-exponential factor used in this estimation was 10^{13} s^{-1}, which is a typical frequency on Si(100) surface. Figure 4.11(b) shows the estimated flip-flop frequency as a function of temperature. Frequent flip motion, approximately

$10^{10}\,s^{-1}$, is induced even at 100 K, and results in the equivalent height of DBs observed in the STM image.

The flip-flop can be explained by the exchange of a lone second-layer atom which is not forming a pair. The recombination of a pair in the second-layer Si atom effectively shifts the position of the lone second-layer Si atom. Fig. 4.12 shows the step by step sequence of flipping showing the recombinations of pairs. This motion of second-layer Si atom is analogous to a soliton in polyacetylene [113] or phason on a clean Si(100) surface [118]. More details of an analogy to polyacetylene is discussed in the next section. We speculate that this motion of the lone Si atom reduces the effective barrier height of flipping, from the solid line in Fig 4.11(b) to the dashed energy curve in the same figure. In our experiments at 40 K, the flip-flop was still present and the two DBs in two-DB structure resulted in equal height.

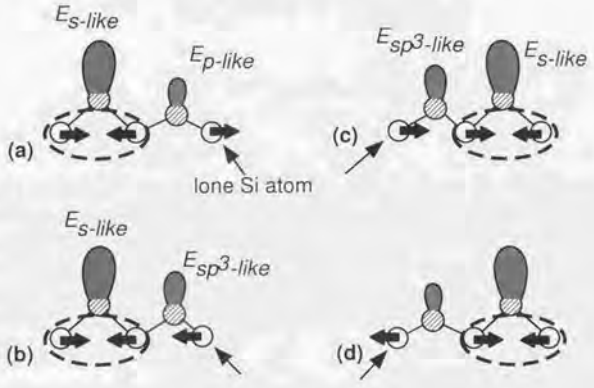

Figure 4.12: Schematics of one-by-one displacements of the second-layer Si positions for two-DB structure. (a)One of the most stable geometry. (b) The right second-layer Si atom is displaced to the left. (c) The center atom is displaced to the right and recombine a new pair. (d) The left second-layer Si atom is displaced to the left, resulting in the most stable geometry which is in mirror symmetry with (a).

In the four-DB structure (Fig. 4.7(c)), the DBs located at both ends are observed to be higher in the filled-state image, but the inner two DBs are observed lower than the edge DBs (Fig. 4.8). Theoretical calculation suggests that two equivalent most-stable configurations exist in mirror symmetry

(these configurations are shown in Figs. 4.13(a) and (b)). In Fig. 4.13(a), the left edge Si atom is the highest and third DB from the left is second highest. We consider again that the frequent flip-flop motion occurs between the two configurations.

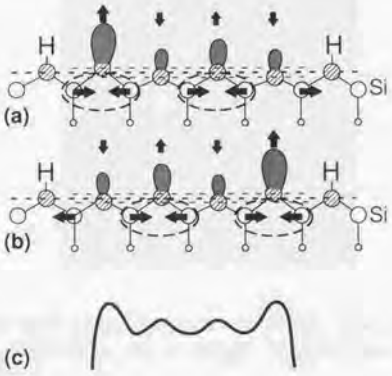

Figure 4.13: Ball-stick models of the four-DB structure showing two possible displacement patterns in a mirror symmetry ((a) and (b)). Blank circles denote Si atoms and gray ovals denote charges in DBs. The dotted oval shows the paired second-layer Si atoms and horizontal dashed lines show the center of the first-layer Si atoms. (c) An expected STM cross-sectional view after considering the flip-flop motion between the two displacement patterns shown in (a) and (b).

Due to the frequent flip-flop motion, the averaged atom height expected for the STM image is higher at the edge DBs and lower at the inner two DBs (Fig. 4.13(c)). This explanation well interprets the STM image

The soliton motion can be quenched at more low temperature. Experimental results at 40 K showed that the soliton motion is restricted at that temperature [119].

However, a question remains. The details regarding the small difference in the heights of the inner two DBs in Fig. 4.8 are not clear yet. To clarify each DB's spatial extent in the direction parallel to the surface, the contrast of the STM image is changed (Fig. 4.14). The STM image clearly shows that the charge extent of the DB pointed by an arrow is smaller than other atom. In consistent with this, the height of this DB is lower than other DBs shown in

Fig. 4.8. A possible explanation is that a stress field associated with surface defects or underlying impurities may affect the soliton (lone second-layer Si atom) motion and thus determine the averaged height differences.

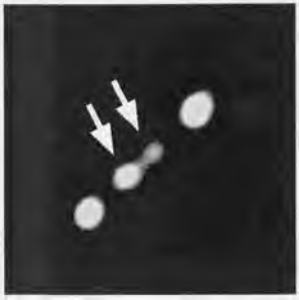

Figure 4.14: An STM image of four-DB structure. The contrast is changed to clarify the spatial extent of the charge. (9 nm×9 nm, V_s = -2.0 V, I_t = 100 pA)

At last, we predict that if much longer even-numbered DB structure (such as made of more than 20 DBs) is fabricated, the DB structure would be fluctuating near the soliton position. It is very interesting to note that this phenomenon is analogous to the solitons in polyacetylene [120] in a sense that the soliton motion determines the structure.

4.3.4 Discussion

In the previous sections, we described how the DB structures made of unpaired DBs, figure out the most stable geometries depending on their length. For the DB structures made of a few DBs, we may say it is a pseudo-molecule. In this case, the electronic band is not formed and discrete energy levels are expected. The charge redistributes in order to remove degeneracy, and this process can be explained by Jahn-Teller effect.

The second-layer Si atoms plays important role in the energy stabilization. The second-layer Si atoms are displaced alternately and form pairs. However, the finite length and odd-even problem prevent the DB structures from taking the simple pairing symmetry.

It is very interesting to note that the soliton-like behavior of a lone silicon atom in even-numbered DB structure is analogous to the solitons [120]

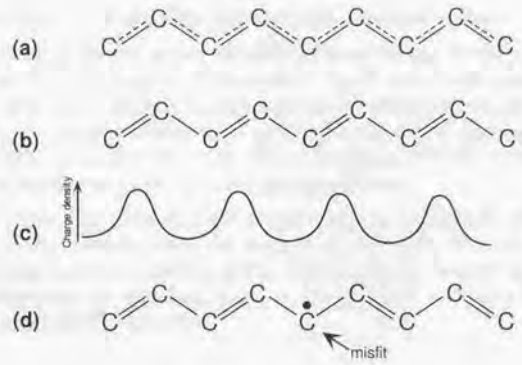

Figure 4.15: (a) Schematic view of a metallic state. (b) Schematic view of a insulating state. (c) Charge density of a π electron. The double bonds have a high density of charge. (d) Misfit in a conjugated chain PA. The black circle denotes the one unpaired π electron. Two adjacent single bonds are touching in this case, and one DB localize near the misfit.

in polyacetylene (PA) [107] I briefly describe the analogy between the polyacetylene and the DB structure.

In Fig. 4.15, the "metallic state" of PA (a) and the transition to the insulating state (b) are illustrated. In the metallic state, the electrons are depicted as delocalized over the entire chain. In the insulating state, there in an alternation of short and long bonds which correspond to double bonds and single bonds, respectively. The π electrons localize at the double bonds (Fig. 4.15(c)).

Due to the Peierls transition, there opens up an energy gap of about 1.7 eV. The Peierls transition occurs at a temperature that is in the same order of magnitude as the gap energy, because above that temperature many electrons are thermally excited across the gap and the solid does not "notice" the gap anymore. Since 1 eV corresponds to a temperature of about 10,000 K, at room temperature PA is far below the Peierls transition. It is not possible to heat PA into the metallic phase, because the polymer decomposes at some hundred degrees centigrate.

There is strict bond alternation in the domains, however, misfits are created at domain boundaries (Fig. 4.15(c)). Actually, misfits are not so well localized and extends over some ten bonds, modifying the bond alternation

gradually [120]. These misfits (domain wall) are called soliton.

A soliton is free to move, because the total energy of the system does not depend on the position of the soliton. As we saw in DB structures, the essence of soliton motion is recombinations of pairs in second-layer Si atom, inducing the charge redistribution and lattice distortion. In similar, the recombinations of π electrons are the soliton motion in PA. The recombinations result in double bond and the C-C spacings change.

If a longer even-numbered DB structure can be fabricated, the structure can be easily predicted from the analogy to a PA. In this case many lone second-layer exists as a soliton in PA. In the domain the pairing of second-layer determines the structure, however, solitons exist at domain boundaries and determined the structure.

4.3.5 Summary

1. Relaxation occurred in a DB structure made of a few unpaired DBs.
2. Length-dependent relaxation was observed.
3. The DB structures can be regarded as pseudo-molecule and a relaxation process is explained by Jahn-Teller distortion.
4. The recombination of second-layer Si atoms are similar to the soliton motion in polyacetylene.

This section is concluded as follows. "Length-dependent relaxation with odd-even problem become apparent in atomic structures."

The determination and prediction of the charge density for even numbers such as six, eight DBs is a challenging theme for both experimental and theoretical calculations.

4.4 Adsorption potential energy surface imaging

Atomic-scale understanding of adsorbate surface migration has the fundamental importance in growth processes of thin films and crystals [122, 123]. As device miniaturization reaches nanometer-length regimes, atomic-level control of the fabrication process is becoming crucial.

Atoms adsorbed on solid surfaces exhibit a wide variety of anisotropic migration due to the surface atomic structures. The interaction of the substrate with the adsorbates determines the potential energy surface (PES), which is of great importance in determining the behavior of the adsorbates.

When the adsorbate atom reaches the surface, the system gains the adsorption energy and the atom is placed at the bottom of a potential well in thermal equilibrium. The thermal fluctuations drive the adsorbate jump laterally along the surface from one well to the next. The direction of each jump is completely random and uncorrelated from jump to jump [132].

Scanning tunneling microscope provides many new studies concerning migration of adsorbates at an atomic level [124]. Much recent attention has been focused on the migration pathway on the surface before the nucleation [125]. Swartzentruber used a noble atom-tracking STM and revealed the adsorption-site resolved 1D migration of Si dimers on a Si(100)2×1 surface [126]. Although many theoretical studies exist, the atomic-scale migration paths are still unexplored experimentally. Thermally deposited Ga atoms migrate on a hydrogen-terminated Si(100)-2×1 surface at room temperature and preferentially adsorb on the dangling bonds [41]. *More detailed understanding of migration process is demanded for the film process and nanostructure fabrication.*

In this section, we show that some of the Ga atoms adsorbed on a hydrogen-terminated Si(100)2×1 surface migrate one-dimensionally, and are imaged as a linear protrusion (Ga-bar structure). The experimental results are analyzed based on the first-principles calculations by Suwa et al. [127]. We find that the Ga atom is confined and migrating in 1D potential well at only narrow range of temperature near 100 K. We point out that the observed height modulation of the Ga-bar structure reflects the local adsorption energy variation, which can be related to the local stress field or charge, induced by surface defects or the local bulk dopants [128].

A Si(100) sample (As-doped, n-type, 7 to 18 mΩ·cm) was cut from a commercial wafer and used as a substrate. Details of the surface and the STM tip preparation [95] have been described in section 3.2 and 3.3. By heating

a Ga metal with W filament to 600 - 650 °C, Ga atoms were evaporated and deposited on Si surface while scanning, at various sample temperatures. A Ga doser was set 10 cm away from the sample and the STM tip. Experiments were carried out at various temperatures ranging from 30 to 150 K, at the Ga deposition in the low-coverage limit.

In order to understand the migration of a Ga atom on a hydrogen-terminated Si(100)-2×1 surface, we performed the first-principles calculations based on a local density functional approach. The basic methods of calculations by Suwa *et al.* are same as that of Watanabe *et al.* [51]. In the calculations, a periodic 4×2 or a 4×4 supercells were used. Wave functions were expanded in a plane-wave basis set with an energy cutoff of 9 Ry. More detailed methods are descibed in section 2.4. In order to obtain PES, the total energy with Ga adsorbate is minimized with respect to the electronic charge density and the substrate lattice. A Ga atom was positioned on appropriate grid points and the electronic structures of the system was calculated. For each position of a Ga atom, the total energy of the system is calculated by optimizing the positions of the other atoms and the vertical position of the Ga atom. The criterion of the convergence of the geometry optimization is that all of the forces acting on each atom are within 1×10^{-3} Hartree/a.u.

4.4.1 Ga-bar structure

Figure 4.16(a) shows the typical gray-scale filled-state STM image after the Ga deposition at 100 K. At this temperature, various types of Ga adsorption are observed: some are on dangling-bonds, at the edge of missing-Si defects, and on the hydrogen-terminated area. Further, we observe many characteristic 1D structures, which we call a Ga-bar structure. Three examples are shown by arrows in Fig. 4.16(a). These structures are formed parallel to the underlying Si dimer rows and are located in the trough between two neighboring Si dimer rows. One of the example is enlarged in Fig. 4.16(b), which is 7.7 nm in length and 0.25 nm in height, and has protrusions at the both end (cross sectional view of the Ga-bar on the Si dimer row structure is shown in Fig. 4.16(c)).

At a glance, we assumed that the Ga-bar structure would be a row of Ga atoms, considering the fact that the formation of ad-dimer chains on a clean Si(100)2×1 surface is quite common, such as the case of Ga [129], Si [130], and Al [54, 131]. They form similar 1D structures of ad-dimers but are perpendicular to the dimer row. Instead, we argue that the Ga-bar structure is an image of a Ga atom adsorbed and migrating one dimensionally as discussed in the following.

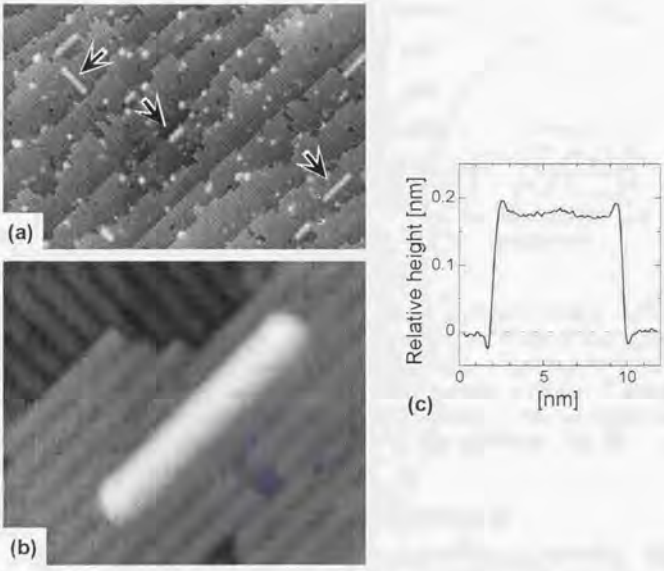

Figure 4.16: (a) A STM image obtained after sub-monolayer Ga deposition at 100 K (70 nm×40 nm, V_s=-2.0 eV, I_t=20 pA)). The white arrows show the characteristic Ga-bar structure. (b) Close up view of a Ga-bar structure (12 nm×9 nm). (c) Cross sectional view of the Ga-bar structure in (b).

First-principles calculations predict that a Ga atom is easy to migrate in a trough. Figure 4.17(a) shows the contour plot of calculated PES for a Ga atom in a 4×2 unit cell. The adsorption sites with lowest potential enegy are located in the trough and the each site is composed of two local minima as are labeled as A_0's in Fig. 4.17(a). An activation barrier between two A_0-site minima is a few meV and negligible at the temperature range of the present experiment. Thus, we regard two A sites as one site throughout this section. We also find a metastable adsorption site with 221 meV higher adsorption potential energy than A_0 site at the pedestal site (between two adjacent dimers which is labeled as B in Fig. 4.17(a)). The Ga atoms adsorbed on hydrogen-terminated surface corresponded to this site. A Ga adsorbate at the A_0 site has lowest activation barrier of 215 meV for surface migration in the direction from A_0 site to A_1 site (path I) in Fig. 4.17(a). The activation

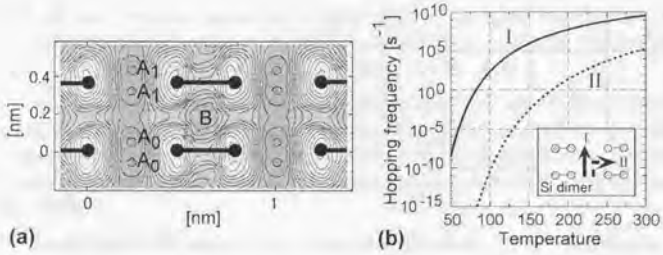

Figure 4.17: (a) Calculated contour plot of potential energy surface (PES) [128]. The contour spacing is 0.1 eV. The zero of the x and y axis are chosen arbitrarily. (b) Temperature dependence of hopping frequency. The solid line shows the hopping rate of the Ga atom along the Si dimer rows. The dashed line shows the hopping rate in the direction perpendicular to the Si-dimer rows (from point A to B in (a)). The inset shows the direction of the diffusion.

barrier from the A site to the B site (path II) is 469 meV.

The migration rate typically depends exponentially on temperature [132]. We evaluate the hopping frequency f using a simple Arrhenius equation.

$$f = \nu \exp(-Q/kT), \tag{4.1}$$

where ν is a pre-exponential factor, Q is an activation barrier for surface migration, k is a Bolzmann constant, and T is the temperature of the system. The pre-exponential factor ν is estimated to be $1.56 \times 10^{13}\,\mathrm{s}^{-1}$ by fitting the calculated PES near hopping site to quadric [127]. Fig. 4.17(b) shows the calculated temperature dependence of hopping frequency f for the Ga migration path I and II shown in the inset of Fig. 4.17(b). For the calculations of both migration path I and II, the same ν is used. Near 100 K, the hopping frequency to the next adsorption site (A_0 site to A_1 site) in the trough (path I) is approximately $100\,\mathrm{s}^{-1}$, whereas for across the dimer row (path II) is $10^{-11}\,\mathrm{s}^{-1}$. As a result of the difference in barrier height, the diffusion becomes anisotropic. These calculations well explain the Ga-bar structure observed in the experiment. From room temperature down to 150 K, a Ga atom migrates two-dimensionally in very fast hopping frequencies for both diffusion paths, which are beyond the time resolution of the STM. Well below 100 K, a Ga atom does not migrate much and we observe stable Ga-bar structure by using STM. This evaluation predicts that the 1D migration of a Ga atom results in the Ga-bar structure, which is observed only in the

narrow range of temperature near 100 K (77 K to 110 K). If it is the case, the Ga-bar structure must be composed of the Ga atom images at the hopping site. The STM image shown in Fig. 4.16(b) has 21 sites.

From our experiments so far, we could not observe any Ga-bar structure at 35 K, 65 K, and 150 K. Observed temperature range was 77 K to 110 K, which agrees with our calculation. This thermal activated process supports that the thermally activated migration is dominant at the sample bias voltage of -2.0 V.

In case of having two or more Ga atoms in the same trough, the theoretical calculation predicts that a Ga dimer would be formed and could be imaged as a Ga-bar structure. However, the probability of having two or more Ga atoms in one Ga-bar structure is very small because the Ga coverage in the present experiment is very low. Thus, we argue that the Ga-bar structure presented in this paper is a image of one Ga atom.

A question arises what terminates the two ends of Ga-bar structure. By applying a voltage pulse and a large tunneling current on a Ga-bar structure (a sample bias voltage of -3.0 V and a tunnenling current of 0.7 nA for 200 ms, for example), the Ga atom move out from the trough and the hydrogen-terminated surface was observed. Figs. 4.18(a) and (b) shows the STM image before and after the pulse. Figure 4.18(b) reveals that the Ga-bar structure is terminated by the dihydride Si dimers (shown by the arrows in (b)) at the both ends. We are able to observe dihydrides at the both ends of the Ga-bar structure also by carefully analyzing the cross sectional view.

The experimental results implies that dihydride act as a hard wall for the Ga-atom migration. Figure 4.18(c) shows the schematic view of the Ga-bar structure and Fig. 4.18(d) shows the calculated cross section of PES along the trough, including a dihydride using a 4×4 unit cell. The plot in Fig. 4.18(c) clearly shows that the dihydride act as a large barrier of about 0.6 eV for Ga-atom migration. Considering the above facts, two dihydrides and a trough form an one-dimensional potential well for the Ga atom. Consequently, we conclude that the Ga-bar structure is an STM image of rapidly migrating Ga atom confined in one-dimensional potential well.

In agreement of theoretical and experimental studies, hopping is essentially confined along the dimer row direction, but limited hopping events across the dimer row was observed. We sometimes observed "split" Ga bar or partially imaged Ga bar. These images are due to the jump occurred between one and subsequent passes of the tip over the Ga bar. Figure 4.19 shows the STM image obtained before hopping (a) and after the hopping (c). The Ga atom has hopped across the dimer row (Fig. 4.19(b))and the Ga bar moved to adjacent dimer row valley. If the both dihydride is in the

same dimer row, equivalent site exist in both side of the dimer row. This valley is also terminated by the dihydride, which means that it is equivalent to the previous valley.

The effect of the tip-sample interactions should be carefully considered. In many other systems, it is likely that the tip-sample interactions affect migration [134]. Sample-biased polarity may also influence the dynamics of adsorbate. However, if a sample is biased negative (filled state), we conclude that the tip-adsorbate interaction is negligible in the present system from the following discussion.

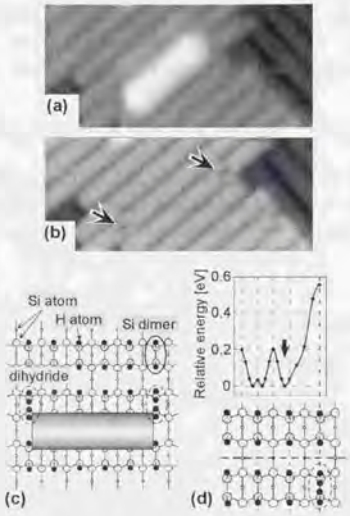

Figure 4.18: STM images of before (a) and after (b) a voltage pulse (7 nm×3 nm, V_s=-2.0 V, I_t=20 pA). Local dihydride species are shown by arrows in (b). (c) Schematic view of a Ga-bar structure. The hatched and blank circles, and filled circles denote the first- and second-layer Si atoms, and hydrogen atoms, respectively. (d) Calculated cross section of the PES along the Ga-bar structure, including dihydride in the 2 × 4 cell.

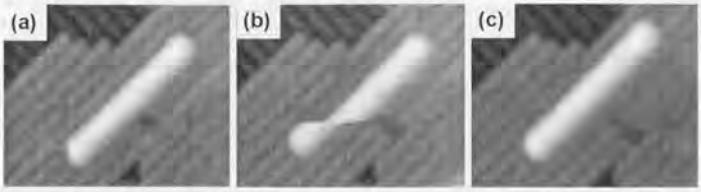

Figure 4.19: A series of filled-state STM image of hopping of Ga atom across the dimer row. (100 K, 12 nm×9 nm, V_s = -2.0 V, I_t = 20 pA). (a) Before the hopping. (b) The hopping event occurred to the left during the scan. (c) After the hopping. Note that the Ga atom has hopped to the adjacent trough.

4.4.2 Probing adsorption potential energy surface

We now extract information of site occupation probability p of a Ga atom at individual adsorption sites from local-height analysis of Ga-bar structure. In the constant-current-mode STM operation, an averaged effective current,

$$p \cdot I = const. \tag{4.2}$$

where I is the peak tunneling current when the Ga atom is under the STM tip. The peak tunneling current I is given by,

$$I = A \exp(-\frac{2\sqrt{2m}}{\hbar}\sqrt{\phi}z), \tag{4.3}$$

where A is a constant, ϕ is the workfunction, when a Ga atom is under the tip, which is estimated to be 5.55 eV from the first-principles calculations, and z is averaged tip to Ga atom spacing, $\hbar$ is the Planck constant divided by 2π, and m is the electron mass, under the WKB approximation [133]. Equations (4.2) and (4.3) implies that the height difference from the reference height can be converted to the ratio of site occupation p.

We analyzed the cross section of the height of the Ga-bar structures and obtained averaged z values (one example is shown in Fig. 4.20(a)). When a Ga-bar structure consists of n adsorption site, the averaged site occupation $\bar{p}$ is given by $1/n$. If the tip-adsorbate interaction is negligible, the visiting possibility under the tip is proportional to the inverse of length. Using this relation, we evaluated z for each Ga-bar structure with different length, using a 10 hopping-site Ga-bar structure as the reference, and it is shown by the dashed curve in Fig. 4.20.

From the plot of the average-height dependence versus length of Ga-bar structure (Fig. 4.20), it is clear that the height of Ga-bar structure decreases as the length increases. This result again supports that the Ga-bar structure is not a row of Ga atom but is related to one-dimensional random-walk hopping in the potential well. In other words, when the length of potential well increases, the probability of Ga atom visiting under the STM tip will decrease. Since the height of STM image reflects time occupancy of Ga atom, the longer Ga-bar structure is observed lower in height. This explanation eliminates the possibility of strong tip-adsorbate interaction, that is, the case of STM tip pushing or pulling the adsorbate, because there should be no length dependence in this case.

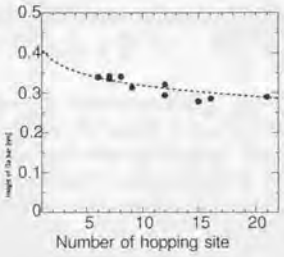

Figure 4.20: Averaged height of Ga-bar structure versus length, obtained at V_s = -2.0 V, I_t = 20 pA.

The estimation is in good agreement with the experimental data, which supports that the tip-adsorbate interaction does not alter the migration at V_s = -2.0 V. Considering these facts, our interpretations of Ga atom are follows. When the sample bias is positive polarity (empty state), the STM tip repel the Ga atom, resulting in fuzzy image. The actual surface potential of Ga on this surface is sum of tip-adsorbate interaction and potential from hydrogen-terminated Si(100) surface. The origin of this tip-adsorbate interaction may be polarization, charge or wind force [135]. We concluded that when the sample bias is negative polarity (filled state), the interaction between the tip and Ga atom is negligible, and the migration is dominated by thermally induced motion. Many studies point out that only either polarity result in negligible tip-adsorbate interaction [25, 26]. For this reason, we stress that Ga-bar height only reflects the local PES, that is, larger time occupancy leads to higher height in STM image.

From this point of view, we again review our data. Equations (4.2) and

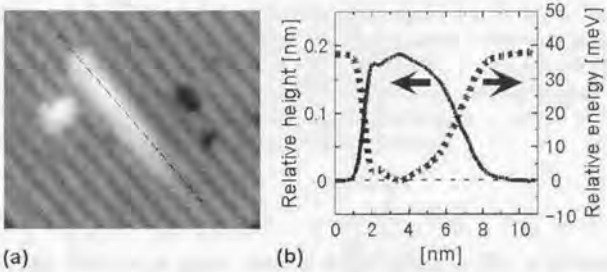

Figure 4.21: Filled-state STM image of gradually-disappearing Ga bar (Ga-comet structure). 11× 9 nm, V_s=-2.0 V, I_t=20 pA.

(4.3) can be applied to each adsorption sites. For the system at the thermal equilibrium, the hopping frequency f and site occupation p follows the relation $p \cdot f = const.$ for each adsorption sites. By assuming that the pre-exponential factor ν is constant for all adsorption sites, we can derive local free-energy variation ΔQ from the local variation of z.

The two dips at the outside of Ga-bar structure in Fig. 4.16(c) correspond to the dihydride. The edge of the Ga-bar structure blocked by the dyhydrides shown by the arrow in Fig. 4.18(b) has $\Delta Q = 4$ meV lower potential energy than adjacent adsorption site. This energy diffence gives the ratio of visiting possibility at the edge to at the adjacent site $= \exp(-\Delta Q/kT) = 1.59$, assuming 100 K and ΔQ is 4 meV. From the previous discussion of visiting possibility vs. height, the height difference is estimated to be 0.018 nm. We observed that the edge of Ga-bar structure is protruded for 0.02±0.003 nm in Fig. 4.16(c), which is in good agreement with the estimation. Further, the cross-section in Fig. 4.16(c) has abroad local maximum in the middle of Ga-bar structure. This local minimum is not a experimental error but appears reproducibly for this particular Ga-bar structure. We believe that there is a local PES distortion in this region. The height of the local minimum is approximately 0.01 nm and this correspond to the potential energy difference of 2.2 meV. The result implies that the center of the Ga-bar structure has PES distortion of 2.2 meV lower that ranges for few nm. In this way, we should be mapping out the local free-energy variation from the height of Ga-bar structure.

We observed gradually disappearing Ga-bar structure which has PES distortion of more than 5 nm. Figure 4.21(a),(b) shows the example of gradually-

disappearing Ga-bar structure (Ga-comet structure) and its cross section, respectively. The height of Ga-comet structure gradually decreases in length scale of about 4 nm in this case, which implies that long-range distortion of potential energy is present. The plot of potential energy difference as a function of the positions in Ga-comet structure is also shown in Fig. 4.21(b). Origins of this distortion is discussed in next section.

4.4.3 Discussion

The origin of the long-range potential energy variation should be carefully considered. A surface strain or a chage induced by defects or step may alter the PES. Swartzentruber pointed out that defects, steps have distorted PES compared with clean Si(100) surface terrace [136]. From the intense STM observations, we concluded that steps and missing-Si defects on surface do not vary the surface potential for such a long range ($\approx$5 nm). In both cases, the Ga-bar structure existed very close to those sites. Other defects observed on hydrogen-terminated surface is dihydride. In section 4.4.2, we described that dihydride distorts potential energy at adjacent dimers. However, no long-range distortion was observed. From the STM observations at V_s = -2.0 V, there were no origin on surface that distorts the potential energy for such a long range. Considering these experimental results, we speculate that the *distortion of potential is due to the sub-surface defects or impurities*, such as dopants.

Electrically active defects in semiconductor crystals have different characteristics, depending on the location of their energy states relative to the conduction- or valence-band edge. Shallow defects have energy levels within a few tens of millielectron volts from the respective band edges, whereas deep defects typically reside within the middle third of the semiconductor energy band gap. Deep levels have highly localized wave functions whereas shallow-level wave functions are as extended as the far reaching Coulomb potential. The dopant in our sample is As which is a shallow defect. Consequently, spatially extended wave functions have a possibility to vary the local PES.

We now estimate the spatial extent of the Coulomb force between shallow donor and an electron. The electron localizes in the proximity of the impurity ion. The Bohr theory of the hydrogen atom is modified to take into account the dielectric constant of the medium and the effective mass of an electron in the periodic potential of the crystal. In the semiconductor, we replace e^2 (e is electron charge) by e^2/ϵ, where ϵ is the static dielectric constant of the medium, and electon mass m by the effective mass m^*. The factor $1/\epsilon$ takes account of the reduction in the Coulomb force between charges caused by

the electronic polarization of the medium.

The Bohr radius of the ground state of hydrogen (a_B) is written as $4\pi\epsilon_0\hbar^2/me^2 = 0.053\,\mathrm{nm}$. Thus, the Bohr radius of the donor a_B^* (nm) is expressed as following equation [137].

$$a_B^* = \frac{4\pi\epsilon_0\epsilon\hbar^2}{m^*e^2} = a_B\frac{m}{m^*}\epsilon = 0.053\frac{m}{m^*}\epsilon$$

Here, $\epsilon_0 = 8.854 \times 10^{-12}\ \mathrm{C^2/N{\cdot}m^2}$ and ϵ is 11.7 for Si.

The application of above equation to silicon is complicated by the anisotropic effective mass of the conduction electrons. To obtain a general impression of the Bohr radius, $m^* \approx 0.19m$ is used. This value is the smallest value for the wave vector in (100) plane. Substituting all the constants gives $a_B^* = 3.26\,\mathrm{nm}$. For futher precise estimation, correct anisotropic mass tesor must be used, however, the estimated a_B^* give us a good value for qualitative discussion.

The above estimation implies that the sub-surface impurities, such as shallow donors or acceptors, have a possibility to vary the potential for at least 3 nm. Considering these results, the possible explanation of the potential energy distortion is that *there exists sub-surface impurity at the tail of Ga-bar comet structure.*

In the Si sub-surface, not only As exists but also O and B exist abundantly. The B-doped p-type Si sample is now prepared and ready for the experiment. Other than impurities, vacancies may have a charge which distorts adsorption potential energy. Any way, it is quite sure that some impurity defect is the origin of the long-range free-energy distortion.

The sub-surface Si dopants in GaAs is reported [138], however, no observation of impurity in Si is reported. We speculate that the impurity or vacancy exist near the Ga comet tail. The existence of the single defect alter the PES. We speculate subsurface impurity play important role on hydrogen-terminated surface.

At last, a brief comment on tip-adsorbate interaction is stated. The field from the STM tip was shown to be negligible in the motion of lead atoms in the vacancies in a Si(100) surface [140]. In many other systems it is likely that the field between the STM tip and the sample will affect motion [121]. In the empty-state image, we could not observe the Ga-bar structure but rather fuzzy image (Fig. 4.22). The solid Ga bar in filled-state STM image has broken up into many lines, which we call fuzzy image. This may be interpreted as that the repulsive force has applied to the Ga atom. The comprehensive understading on interaction of STM tip and the Ga atom at sample-positive bias is still in mystery.

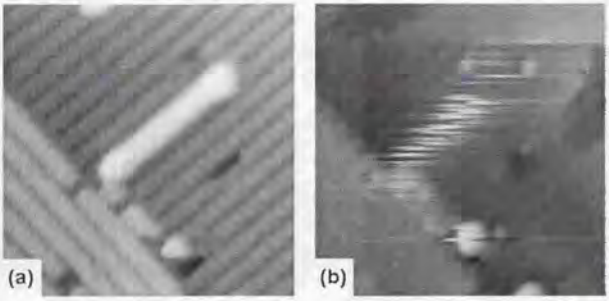

Figure 4.22: (a) Filled- (V_s = -2.0 V) and (b) empty- (V_s = +2.0 V) state STM images of Ga bar (10 nm×10 nm, I_t = 20 pA).

4.4.4 Summary

The main results presented in this section are:

1. A Ga atom migrates in a 1D potential well confined by adjacent dimer rows and local dihydride defects at near 100 K.
2. The height mapping of Ga-bar structure is a local probe of the adsorption free-energy variation, and can be used as quantitative studies.
3. The origin of the long-range (≈5 nm) adsorption free-energy variation may be a sub-surface impurity.

The conclusion of this section is:

"Quantitative studies of adsorption free-enegy variation is possible using the Ga-bar structure as a local probe. Sub-surface impurities may distort the free-energy."

Chapter 5

Conclusions and outlook

From the present study, following conclusions were derived.

In conclusion, we fabricated atomic-scale DB structures by extracting individual hydrogen atoms from the hydrogen-terminated Si(100)2×1-H surface at around 100K. Charge redistribution was observed for the DB wires made of unpaired DBs. We compared the results with the first-principles calculations and concluded that the origin of this redistribution is similar to Peierls distortion. For the DB wire made of DB pairs, a buckling structure was observed. The DB structure made of both paired and unpaired DB show finite DOS at E_F. It is interesting to note that the electronic structure reflects the subtle difference in atomic scale DB configurations. The STM/STS results enable us to distinguish the changes in electronic structures depending on the DB configurations. We believe that the DB structures on the hydrogen-terminated Si surface provide us with unique and stimulating systems for the study of pseudo-one-dimensional atomic-scale structures.

The atomic structures made of unpaired DBs on a hydrogen-terminated Si(100) 2×1 surface shows interesting similarity in the relaxation process with molecules, such as polyacetylene. Thus, we may call the structure as artificial pseudo-molecules. The interesting properties include well-known Jahn-Teller distortion and soliton motion in the molecules. These DB structure has advantages in the points that it can be fabricated on the surface and that the solitons can possibly be controlled.

The results imply that this stabilization can be also found not only in DB structures but also in other artificial 1D atomic structures.

The ability to handle atoms one by one suggests that molecular synthesis is possible with the STM. This will be a very big impact to bio-technology and chemistry. STM is not only a tool to observe atoms and electronic structures,

but in the near future, it will become an atom manipulating apparatus.

Although the present study involves the Si(100) surface, the same arguments may well be applied to a variety of systems.

Atomic structures, such as defects, individual dopants, and artificial atomic structures, in semiconductors will continue to attract scientific and technological interest. The properties of defects have to be understood so that the defects can either be eliminated or introduced. The dimension shrinking of semiconductor structures will also require ever more sensitive and selective characterization tools.

Letters of thanks

I would like to express my sincere gratitude to the following supervisors, collaborators, and supporters.

Family

Kiyomi, Goro and Masaru Hitosugi

I appreciate you more than you'll ever know. Thank you for your heart-warming support.

Supervisors

Prof. Koichi Kitazawa (University of Tokyo)

I am grateful to you for giving me many pieces of valuable advice, especially concernig how I should perform "*science*." Thank you for giving me an opportunity to do research with the scientists in Hitachi, Ltd.

Dr. Tomi Hashizume (Hitachi, Ltd.))

On numerous occasions you gave me precise and timely advice. Thank you for taking care of me and for nutrition supplement.

Prof. Tetsuya Hasegawa (Tokyo Institute of Technology)

Thank you for taking care of me for total of six years and for valuable discussions.

Advisors and Collaborators

Prof. Satoshi Watanabe (University of Tokyo)

Thank you for your valuable calculations and fruitful discussions.

Mr. Seiji Heike (Hitachi, Ltd.)

You are a talented guy and I learned many things from you. It's been a pleasure working with you.

Dr. Zhi-qiang Li, Prof. Kaoru Ohno, Prof. Yoshiyuki Kawazoe (University of Tohoku)

Your calculations have revealed many things which my experiments could not clarify. Thank you very much.

Dr. Yuji Suwa (Hitachi, Ltd.)

Thank you for stimulating discussions and your calculations.

Ms. Shinobu Matsuura (University of Tokyo)

Thank you for experimental assistance and your data.

Dr. Toshiyuki Onogi, Dr. Masahiko Ichimura (Hitachi, Ltd.)

Without fruitful discussions with you, the research would not have been possible. Thank you very much.

Dr. Hiroshi Kajiyama, Mr. Mashayoshi Ishibashi

Thank you for valuable discussions.

I also thank researchers and support staffs of Advance Research Laboratory, Hitachi Ltd.

Management and Support staff

Dr. Yasuo Wada (Hitachi, Ltd.)

You gave me a marvelous chance to do experiments at Advanced Research Laboratory, Hitachi, Ltd. Thank you very much.

Dr. Katsuki Miyauchi (Hitachi, Ltd.)

Thank you for not only being a manager but also encouraging me on numerous occasions and sometimes "beer friend."

Technicians in Technical Support Center (Advanced research laboratory, Hitachi, Ltd.)

Thank you for supporting me on experimental apparatuses.

Dr. Ayumu Kida

Thank you for continuous encouragement.

I specially thank Ms. Michiyo Asaka for her heart-warming sincere support.

All my friends

Thanks a lot!

Reference

[1] R. H. Dennard, F. H. Gaensslen, H. -N. Yu, V. L. Rideout, E. Bassous, A. R. LeBlanc, IEEE Journal of Solid-State Circuits, SC-9, 256 (1974).

[2] S. M. Sze, *Physics of Semiconductor Devices*, (John Wiley & Sons, 1981).

[3] P. Gagini, J. Glaze, O. Williams, *Solid State Technology*, January 1998, p.73.

[4] A. S. Grove, *Physics and Technology of Semiconductor Devices*, (Wiley, New York, 1968)

[5] T. Sugano, *VLSI Process Data Handbook*, (Science Forum, Tokyo, 1990); R. W. Keyes, Phys. Today 45, 42 (1992)

[6] H. Sakaki, Jpn. J. Appl. Phys. 19, L735 (1980); H. Sakaki, Jpn. J. Appl. Phys. 28, L314 (1989).

[7] *Mesoscopic Phenomena in Solids*, edited by B. L. Al'tshuler, P. A. Lee, R. A. Webb, (North-Holland, Amsterdam, 1991).

[8] K. Yano, T. Ishii, T. Hashimoto, T. Kobayashi, F. Murai, K. Seki, *Technical Digest, IEEE International Electron Devices, Meeting*, 541, (IEEE, New York, 1993).

[9] G. Binnig, H. Rohrer, Ch. Gerber, E. Weibel, Phys. Rev. Lett. 49, 57 (1982).

[10] General reviews: G. Binnig, H. Rohrer, Rev. Mod. Phys. 59, 615 (1987); P. K. Hansma, J. Tersoff, J. Appl. Phys. 61, R1 (1987).

[11] J. Tersoff, D. R. Hamann, Phys. Rev. Lett. 50, 1998 (1983); Phys. Rev. B 31, 805 (1985).

[12] R. M. Feenstra, J. A. Stroscio, J. Tersoff, A. P. Fein, Phys. Rev. Lett. 58, 1192 (1987).

[13] R. Wiesendanger, *Scanning Probe Microscopy and Spectroscopy*, (Cambridge University Press, Cambridge, 1994).

[14] R. Feynman, J. Microelectromechanical Systems 1, 60 (1992); R. Feynman, J. Microelectromechanical Systems 2, 4 (1993).

[15] *Nanowires*, edited by P. A. Serena, N. Garcia, (Kluwer Academic Publishers, The Netherlands, 1997); *Atomic and Molecular Wires*, edited by C. Joachim, S. Roth, (Kluwer Academic Publishers, The Netherlands, 1997)

[16] B. J. van Wees, H. van Houten, C. W. J. Beenakker, J. G. Williamson, L. P. Kouwenhoven, D. van der Marel, C. T. Foxon, Phys. Rev. Lett. 60, 848 (1988); D. A. Wharam, T. J. Thornton, R. Newbury, M. Pepper, H. Ahmed, J. E. F. Frost, D. G. Hasko, D. C. Peacock, D. A. Ritchie, G. A. C. Jones, J. Phys. C21, L209 (1988).

[17] See, for example, G. D. Mahan, *Many-particle Physics*, (Plenum, New York, 1990).

[18] See, for example, C. F. Quate, *Manipulation and modification of nanometer scale objects with the STM, Highlights in condensed matter physics and Future Prospects*, edited by L. Esaki, (Plenum, New York, 1991).

[19] Ph. Avouris, Acc. Chem. Res. 28, 95 (1995).

[20] J. A. Stroscio, D. M. Eigler, Science 254, 1318 (1991).

[21] R. S. Becker, J. A. Golovchenko, B. S. Swartzentruber, Nature 325, 419 (1987).

[22] D. M. Eigler and E. K. Schweizer, Nature 344, 524 (1990); Other examples of atomic manipulations can be seen in http://www.almaden.ibm.com/st/.

[23] M. F. Crommie, C. P. Lutz, D. M. Eigler, Science 262, 218 (1993).

[24] J. J. Boland, Science 262, 1703 (1993).

[25] Ph. Ebert, M. G. Lagally, K. Urban, Phys. Rev. Lett. 70, 1437 (1993).

[26] L. J. Whitman, J. A. Stroscio, R. A. Dragoset, R. J. Cellota, Science 251, 1207 (1991).

[27] R. M. Ostrom, D. M. Tanenbaum, A. Gallagher, Appl. Phys. Lett. 61, 925 (1992).

[28] S. Heike, T. Hashizme, Y. Wada, Jpn. J. Appl. Phys. 34 L1061 (1995).

[29] L. Bartels, G. Meyer, K. -H. Rieder, Phys. Rev. Lett. 79, 697 (1997).

[30] H. J. Mamin, P. H. Guethner, D. Ruger, Phys. Rev. Lett. 65, 2418 (1990); H. J. Mamin, S. Chiang, H. Birk, P. H. Guethner, D. Ruger, J. Vac. Sci. Technol. B9 1398 (1991).

[31] R. M. Silver, E. E. Ehrlich, A. L. de Lozanne, Appl. Phys. Lett. 51, 247 (1997).

[32] W. Li, J. A. Virtanen, R. M. Penner, Appl. Phys. Lett. 60, 1181 (1992).

[33] H. Kuramochi, H. Uchida, M. Aono Phys. Rev. Lett. 72, 932 (1994).

[34] I. -W. Lyo, Ph. Avouris, Science 253, 173 (1991).

[35] M. Aono, A. Kobayashi, F. Gray, H. Uchida, D. -H. Huang, Jpn. J. Appl. Phys. 32, 1470 (1993); D. Huang, H. Uchida. M. Aono, J. Vac. Sci. Technol. B12, 2429 (1994).

[36] T. H. P. Chang, D. P. Kern, E.Kratschmer, K. Y. Lee, H. E. Luhn, M. A. McCord, S. A. Rishton, Y. Vladimirsky, IBM J. Res. Develop. 32, 462 (1988).

[37] J. A. Dagata, J. Schneir, H. H. Harary, C. J. Evans, M. T. Postek, J. Bennett, Appl. Phys. Lett. 56, 2001 (1990).

[38] M. Kasu, T. Makimoto, N. Kobayashi, Jpn. J. Appl. Phys. 36, 3821 (1997).

[39] S. Hosoki, S. Hosaka, T. Hasegawa, Appl. Surf. Sci. 60/61, 643 (1992).

[40] J. W. Lyding, T. -C. Shen, J. S. Hubacek, J. R. Tucker, G. C. Abeln, Appl. Phys. Lett. 64, 2010 (1994).

[41] T. Hashizume, S. Heike, M. I. Lutwyche, S. Watanabe, K. Nakajima, T. Nishi, Y. Wada, Jpn. J. Appl. Phys. 35, L1085 (1996).

[42] D. P. Adams, T. M. Mayer, B. C. Swartzentruber, J. Vac. Sci. Technol. B 14, 1642 (1996).

[43] T. -C. Shen, C. Wang, J. R. Tucker, Phys. Rev. Lett. 78, 1271 (1997).

[44] M. Sakurai, C. Thirstrup, M. Aono, unpublished.

[45] J. W. Lyding, G. C. Abeln, T. -C. Shen, C. Wang, J. R. Tucker, J. Vac. Sci. Technol. B12, 3735 (1994).

[46] H. Kajiyama, S. Heike, T. Hitosugi, T. Hashizume, Jpn. J. Appl. Phys. 37, L1350 (1998).

[47] S. Watanabe, Y. A. Ono, T. Hashizume, Y. Wada, Surf. Sci. 386, 340 (1997).

[48] M. F. Crommie, C. P. Lutz. D. M. Eigler, Nature 363, 524 (1993).

[49] S. Heike, S. Watanabe, Y. Wada, T. Hashizume, Phys. Rev. Lett. 81, 890 (1998).

[50] C. Thirstrup, M. Sakurai, K. Stokbro, M. Aono, submitted to Phys. Rev. Lett.

[51] S. Watanabe, Y. A. Ono, T. Hashizume, Y. Wada, Phys. Rev. B54, R17308 (1996).

[52] S. Watanabe, M. Ichimura, T. Onogi, Y. A. Ono, T. Hashizume, Y. Wada, Jpn. J. Appl. Phys. 36, L929 (1997); M. Ichimura, K. Kusakabe, S. Watanabe, T. Onogi, submitted.

[53] M. J. Haye, P. M. L. O. Scholte, A. F. Bakker, S. W. de Leeuw, F. Uinistra, G. Brocks, Phys. Rev. B 56, R1708 (1997).

[54] G. Brocks, P. J. Kelly, R. Car, Phys. Rev. Lett. 70, 2786 (1993).

[55] N. D. Lang, Phys. Rev. Lett. 79, 1357 (1997).

[56] N. D. Lang, Phys, Rev. B52, 5335 (1995).

[57] T. Yamada, Y. Yamamoto, Phys. Rev. B54, 1902 (1996).

[58] X. Bouju, C. Joachim, C. Girard, Phys. Rev. B50, 7893 (1994).

[59] P. von Allmen, K. Hess, Phys. Rev. B52, 5243 (1995).

[60] T. Hashizume, to be published.

[61] H. Nejoh, D. Fujita, H. Sheng, T. Uchihashi, U. Ramsperger, S. Odasso, D. Rogers, H. Okamoto, Z. -C. Dong, T. Yakabe, T. Ohki, K. Amemiya, Y. Sozu, Hyoumen Kagaku in Japanese, 19, 727 (1998).

[62] C. -S. Jiang, T. Nakamura, T. Okuda, M. Aono, to be published.

[63] H. Rohrer, priv. commun. I also had same opinion with him.

[64] R. E. Schlier, H. E. Farnworth, J. Chem. Phys. 30, 917 (1959).

[65] J. A. Appelbaum, G. A. Baraff, D. R. Hamman, Phys. Rev. B14, 588 (1976); J. A. Appelbaum, D. R. Hamman, Surf. Sci. 74, 21 (1978).

[66] D. Haneman, Phys. Rev. 121, 1093 (1961); W. A. Harrison, Surf. Sci. 55, 1 (1976).

[67] *Hyoumen ni okeru Riron* I, in Japanese, edited by M. Tsukada, p. 126, (Maruzen, 1994).

[68] C. B. Duke, in *Physical Structure, Handbook of Surface Science*, edited by W. N. Unertl, Vol. 1, (Elsevier, North Holland) p.229.

[69] Q. -K. Xue, T. Hashizume, T. Sakurai, Prog. Surf. Sci. 56, 1 (1997).

[70] D. J. Chadi, Phys. Rev. Lett. 43, 43 (1979).

[71] R. M. Tromp, R. J. Hamers, J. E. Demuth, Phys. Rev. Lett. 55, 1303 (1985); R. J. Hamers, R. M. Tromp, J. E. Demuth, Phys. Rev. B 34, 5343 (1986).

[72] R. A. Wolkow, Phys. Rev. Lett. 68, 2636 (1992).

[73] J. J. Boland, Adv. Phys. 42, 129 (1993).

[74] J. Pollman, P. Kruger, A. Mazur, J. Vac. Sci. Technol. B5, 945 (1987).

[75] A. Redondo, W. A. Goddard, J. Vac. Sci. Technol. 21, 344 (1982).

[76] A. Ramstad, G. Brocks, P. J. Kelly, Phys. Rev. B 51, 14504 (1995).

[77] J. J. Boland, Phys. Rev. Lett. 65, 3325 (1990).

[78] T. Sakurai, H. D. Hagstrum, Phys. Rev. B 14, 1593 (1976); S. Maruno, H. Iwasaki, K. Horioka, S. T. Li, S. Nakamura, Phys. Rev. B 27, 4110 (1983).

[79] J. J. Boland, Phys. Rev. Lett. 67, 1539 (1991).

[80] S. Watanabe, Y. A. Ono, T. Hashizume, Y. Wada, J. Yamaguchi and M. Tsukada, Phys. Rev. B52, R10768 (1995).

[81] D. M. Ceperley, B. J. Alder, Phys. Rev. Lett. 45, 566 (1980).

[82] J. P. Perdew, A. Zunger, Phys. Rev. B23, 5048 (1981).

[83] D. Vanderbilt, Phys. Rev. B41, 7892 (1990).

[84] K. Laasonen, A. Pasquarello, R. Car, C. Lee, D. Vanderbilt, Phys. Rev. B 47, 10142 (1993).

[85] O. Sugino, A. Oshiyama, Phys. Rev. Lett. 68, 1858 (1992); J. Yamauchi, M. Tsukada, S. Watanabe, O. Sugino, Phys. Rev. B54, 5586 (1996).

[86] N. Hamada, *Baruku no densi-jyoutai* in Japanese, edited by R. Yamamoto, (Kaibun-do, 1990).

[87] Many techniques concerning LT-UHV STM are reported. See, for example, J. H. Ferris, J. G. Kushmerick, J. A. Johnson, M. G. Yoshikawa Youngquist, R. B. Kessinger, H. F. Kingsbury, P. S. Weiss, Rev. Sci. Inst. 69, 2691 (1998); G. Meyer, Rev. Sci. Inst. 67, 2960 (1996).

[88] See, for example, Cryogenics 29, 857 (1989); Rev. Sci. Inst. 60, 3315 (1989); Rev. Sci. Inst. 57, 404 (1986).

[89] A. J. Melmed J. Vac. Sci. Technol. B9 (2), Mar/Apr 1991.

[90] H. Bourque, R. M. Leblanc Rev. Sci. Instrum. 66(3), (1995).

[91] See, for example, *Scanning Tunneling Microscopy*, edited by J. A. Stroscio, W. J. Kaiser, p. 52 (Academic Press Inc., 1993).

[92] See, for example, T. T. Tsong, *Atom-Probe Field Ion Microscopy*, (Cambridge University Press, 1990); T. T. Tsong, Physics Today, May 1993, p.24; T. Sakurai, T. Hashizume, I. Kamiya, Y. Hasegawa, N. Sano, H. W. Pickering, A. Sakai, Prog. Surf. Sci. 33, 3 (1990); T. Hashizume, Y. Hasegawa, I. Kamiya, T. Ide, I. Sumita, S. Hyodo, T. Sakurai, H. Tochihara, M. Kubota, Y. Murata, J. Vac. Sci. Technol. A8, 233 (1990).

[93] S. Watanabe, M. Aono, M. Tsukada, Jpn. J. Appl. Phys. 32, 2911 (1993).

[94] T. Sakurai, M. J. Cardillo, H. D. Hagstrum, J. Vac. Sci. Technol. 14, 397 (1977).

[95] T. Hitosugi, T. Hashizume, S. Heike, S. Watanabe, Y. Wada, T. Hasegawa, K. Kitazawa, Jpn. J. Appl. Phys. 36, L361 (1997).

[96] T.-C. Shen, C. Wang, G. C. Abeln, J. R. Tucker, J. W.Lyding, Ph. Avouris, R. E. Walkup, Science 268, 1590 (1995).

[97] R. E. Walkup, D. M. Newns, Ph. Avouris, in *Atomic and Nanometer-Scale Modification of Materials: Fundamentals and Applications*, edited by Ph. Avouris (Kluwer, Dordrecht, 1993), pp. 97-109.

[98] D. Huang, Y. Yamamoto, Jpn. J. Appl. Phys. 35, 3734 (1996).

[99] K. Stokbro, C. Thirstrup, M. Sakurai, U. Quaade, B. Y. -K. Hu, F. P. Murano, F. Gray. Phys. Rev. Lett. 80, 2618 (1998).

[100] M. McEllistrem, M. Allgeier, J. J. Boland, Science 279, 545 (1998).

[101] J. H. Owen, D. R. Bowler, C. M. Goringe, K. Miki, G. A. Briggs, Phys. Rev. B. 54, 14153 (1996).

[102] A. Vittadini, A. Selloni, M. Casarin, Surf. Sci. 289, L625 (1993).

[103] E. T. Foley, A. F. Kam, J. W. Lyding, Ph. Avouris, Phys. Rev. Lett. 80, 1336 (1998).

[104] P. E. Peierls, *Quantum Theory of Solids*, (Oxford University Press, London, 1955) p. 108.

[105] S. Watanabe, priv. comm.

[106] J. A. Wilson, F. J. DiSalvo, S. Mahajan, Phys. Rev. Lett. 32, 882 (1974).

[107] *An Introduction to Molecular Electronics*, edited by M. C. Petty, M. R. Bryce, D. Bloor. (Edward Arnold, 1995).

[108] S. Watanabe, priv. commun.

[109] P. W. Anderson, Phys. Rev. 109, 1492 (1958).

[110] *Organic Conductors*, edited by J. P. Farges, p.659, (Macel Dekker, Inc. New York).

[111] S. Tarucha et al., Solid St. Comm. 94, 413 (1995).

[112] H. A. Jahn, E. Teller, Proc. Roy. Soc. (London) A161, 220 (1937).

[113] W. P. Su, J. R. Shrieffer, A. J. Heeger, Phys. Rev. Lett. 42, 1698 (1979). W. P. Su, J. R. Shrieffer, A. J. Heeger, Phys. Rev. B22, 2099 (1979); A. J. Heeger *et al.*, Rev. Mod. Phys. 60, 781 (1988).

[114] T. Hitosugi *et al.*, submitted to Phys. Rev. Lett.

[115] Z. -Q. Li, K. Ohno, Y. Kawazoe *et al.*, unpublished.

[116] G. Kress, J. Furthmuller, Phys. Rev. B54, 11169 (1996).

[117] L. Salem, *The Molecular Orbital Theory of Conjugated Systems*, (W. A. Benjamin Inc., New York, 1966).

[118] H. Shigekawa, K. Miyake, M. Ishida, K. Hata, H. Oigawa, Y. Nannichi, A. Kawazu, R. Yoshizaki, T. Abe, T. Ozawa, T. Nagamura, Jpn. J. Appl. Phys. 35, L1081 (1996).

[119] Hitosugi *et al.*, to be submitted to Phys. Rev. B.

[120] S. Stafström and K. A. Chao, Phys. Rev. B29, 7010 (1984).

[121] J. Li, R. Berndt, W. -D. Schneider, Phys. Rev. Lett. 76, 1888 (1996).

[122] W. K. Burton, N. Cabrera, F. C. Frank, Philos. Trans. R. Soc. London. Ser. A 243, 299 (1951); Z. Zhang, M. G. Lagally, Science 276 (1997) 377.

[123] *Epitaxial Growth*, edited by J. D. Mathews, (Academic, New York, 1975); *Kinetics of Ordering and Growth at Surfaces*, edited by M. G. Lagally, (Plenum, New York, 1990). M. G. Lagally, Physics Today, November 1993, page 24.

[124] Y. -W. Mo, R. Kariotis, B. S. Swartzentruber, M. B. Webb, M. G. Lagally, J. Vac. Sci. Technol. A 8, 201, (1990).

[125] G. Brocks, P. J. Kelly, R. Car, Phys. Rev. Lett. 66, 1729 (1991).

[126] B. S. Swartzentruber, Phys. Rev. Lett. 76 (1996) 459.

[127] Y. Suwa et al. unpublished.

[128] T. Hitosugi, Y. Suwa, S. Matsuura, S. Heike, T. Hashizume , S. Watanabe, T. Hasegawa, K. Kitazawa, to be submitted to Phys. Rev. Lett.

[129] J. Nogami, S. Park, C. F. Quate, Appl. Phys. Lett. 53, 2086 (1988).

[130] Y. M. Mo, J. Kleiner, M. B. Webb, M. G. Lagally, Phys. Rev. Lett. 66, 1998 (1991).

[131] J. Nogami, A. A. Baski, C. F. Quate, Phys. Rev. B44, 1415 (1991).

[132] A. Zangwill, *Physics at Surfaces*, (Cambridge University Press, 1988), p. 375

[133] J. G. Simmons, J. Appl. Phys. 35, 2472 (1964).

[134] J. Li, R. Berndt, W. -D. Schneider, Phys. Rev. Lett. 76, 1888 (1996).

[135] A. Buldum, S.Ciraci, Phys. Rev. B 54, 2175 (1996); D. M. Eigler and E. K. Schweizer, Nature 344, 524 (1990).

[136] B. S. Swartzentruber, Surf. Sci., 386, 195 (1997).

[137] See, for example, *Introduction to Solid State Physics*, 7th edition, C. Kittel, (John Wiley & Sons, Inc, New York, 1986); *Handoutai no Butsuri* in Japanese, p.106, N. Mikoshiba, (Baifu-kan, 1991)

[138] M. C. M. M. van der Wielen, A. J. A. van Roij, H. van Kempen, Phys. Rev. Lett. 76, 1075 (1996).

[139] Y. M. Mo, M. G. Lagally, Surf. Sci. 248 (1991) 313. (SAGASU)

[140] N. Kitamura, M. G. Lagally, M. B. Webb, Phys. Rev. Lett. 71, 2082 (1993).

Following books were frequently referred.

- N. W. Ashcroft, N. D. Mermin, *Solid State Physics*, (Holt, Rinehart and Winston, New York, 1976).
- R. Wiesendanger, *Scanning probe microscopy and spectroscopy*, (Cambridge University Press, Cambridge, 1994).
- *Scanning tunneling microscopy*, edited by J. A. Stroscio, W. J. Kaiser, (Academic Press, Inc., 1993).
- A. Zangwill, *Physics at Surfaces, (Cambridge University Press, Cambridge, 1988).*
- S. Roth, *One-Dimensional Metals*, (VCH, 1995).

Appendix A

Abstract in Japanese

はじめに

固体物理の分野で原子スケールの物理が非常に大きな関心を集めている。その背景として、半導体技術の急速な進歩により、ナノメータスケールの非常に微細なデバイスの開発が試みられるようになったことがあげられる。さらに、低次元系において量子ホール効果やラッティンジャー液体等の現象が脚光を浴び、原子スケール構造中でのこれら物理現象の振る舞いも関心が持たれている。また、走査トンネル顕微鏡 (STM) 技術の発展により原子を表面で自在に操ることが可能となり、作製した原子構造の物性を評価することが可能になってきたことも背景としてあげられる。本研究では微細な構造・領域の表面物性を理解することを目的として、STM を用い、水素終端 Si(100)2×1 表面上に作製した原子スケール構造の物性評価と、Ga 原子の吸着ポテンシャルエネルギー (吸着原子の基板表面上で感じるポテンシャルエネルギー) の空間分布測定に関する実験を行った。さらに、大型計算機を用いた第一原理計算 (局所密度汎関数法) による物性研究グループの協力を得て、作製した原子構造の物性を理解し、これから作るべき構造の設計および物性の予測を行ないつつ研究を進めた。

本研究は大きく分けて以下の二つの研究から成り立っている。

1. ダングリングボンド構造の電子状態と構造緩和
   一原子幅の原子細線は電気伝導するのか、という大きな疑問に対して実験的な挑戦が非常に盛んである。そのような実験に関連して、STM を用いて水素終端 Si(100)2×1 表面上にダングリングボンド (DB) からなる原子スケール構造を作製し、そのトンネルスペクトルおよび電子状態密度の空間分布を測定した。そして第一原理計算の結果と比較して、実際に原子スケール構造を作るとどのように構造安定化を起こすのか、また、それに伴う電子状態の変化について議論する。

2. 吸着ポテンシャルエネルギーの空間分布観察
   固体表面における原子の吸着・表面拡散・脱離などについての研究が、薄膜成長

や触媒作用のメカニズムに関連して幅広く行われている。基板表面での原子の動きは表面と原子間の吸着ポテンシャルエネルギー面 (PES) に支配されおり、その知見を実験的に得ることが非常に重要である。しかし吸着 PES のナノメータスケールでの空間分布測定はいまだ皆無といってよい。本研究では水素終端 Si(100)2×1 表面上の Ga 原子像が吸着 PES を反映することを示し、その空間分布を議論する。

すべての実験は超高真空 STM を用い、室温および低温 (30 K～200 K) で測定を行った。As ドープした Si(100)(7～18 mΩ·cm) を試料基板とし、探針はタングステンを電解研磨して自作した。水素終端 Si(100)2×1 表面に観察時より大きなトンネル電流とバイアス電圧を印加しながら STM 探針を移動させることにより、水素原子を引き抜いて DB 構造を作製した。

ダングリングボンド構造の電子状態と構造緩和

水素終端 Si(100)2×1 表面には、paired DB(Si ダイマーから二つの水素が抜けたもの) と unpaired DB(Si ダイマーから水素が一つ抜けたもの) の 2 種類の DB が存在する (図 1(a))。それら DB をダイマー列に沿って並べた、長さ数 nm から十数 nm の 3 種類の構造:(A) paired DB のみ、(B) unpaired DB のみ、そして (C) それら両者がランダムに混在した構造を作製し、STM/STS 観察を行なった [95]。無限の長さの DB 構造を仮定して得られた第一原理計算 [51] と比較した結果を表に示す。

	実験 (STM/STS 観察)	第一原理計算 (密度汎関数法)
(A) paired DB のみ	清浄 Si(100)2×1 表面と同様の非対称ダイマーが観察される。エネルギーギャップ E_g=0.5 eV。	非対称ダイマーと半導体的なバンド構造 (E_g=0.5 eV) が予測される。
(B) unpaired DB のみ	構造緩和と電荷再分布が起きたため、DB が一つおきに観察される。図 1(b) に STM 像を示す。	バイエルス歪みが起きて構造緩和。その緩和の仕方は実験と非常によく一致している。E_g=0.025 eV。
(C) 両者がランダムに混在した構造	フェルミ準位に有限な状態密度が存在する。	計算なし。

表　3 種類の DB 構造についての実験結果と計算結果の比較

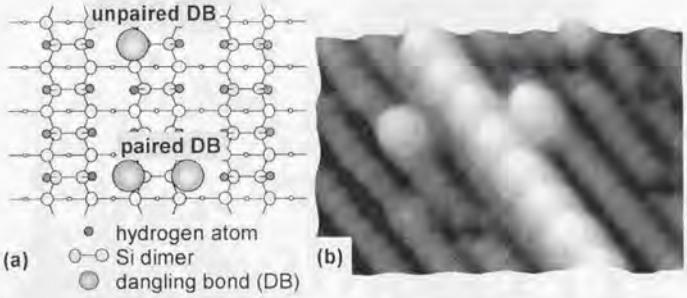

Figure A.1: (a) 水素終端 Si(100)2×1 表面の模式図。(b)unpaired DB のみからなる構造の STM 像 (7 nm×4 nm, サンプルバイアス V_s = -2.0 V, トンネル電流 I_t = 20 pA, 96 K)。

以上の考察から、次の結論が導き出された。

1. unpaired DB または paired DB のみが連なった構造のように、長さが数 nm 程度であっても、周期的な原子構造と見なせるものについては構造緩和が起き、それに伴い電荷が再分布してエネルギーギャップを持つようになる。

2. フェルミ準位に有限な状態密度を持つ構造にするためには、単原子幅と二原子幅の原子構造をランダムに混ぜるのがよい。

比較的長い構造 (数 nm から十 nm 程度) では緩和が起きることがわかり、無限大の長さを持った DB 構造の第一原理計算と良い一致を示した。それでは数個の unpaired DB が並んだ構造はどのような緩和を示すのであろうか。100 K 付近でダイマー列に平行に unpaired DB が並んだ構造の STM 観察を行うと、DB の高さに差が出ることを見いだした [114]。2,3,4,5 個の DB で構成した列 (2-DB 構造, 3-DB 構造, ・・・と今後呼ぶ) の断面図を図 2(a) に示す。断面図は V_s = -2.0 V(占有状態)、I_t = 20 pA で測定した。

2-DB 構造は高さの差はないが、3-DB 構造では両端の DB に比べ中心の DB が低く観察される (図 2(b))。4-DB 構造の場合には両端の DB は同じ高さだが、中心の 2 つの DB が低く観察されている。5-DB 構造では両端のピークと中央にもう一つピークが存在する。このような原子数個分の構造中で起きる緩和は、長さの効果や両端の効果が効いてくることが予想され、周期的に DB が並んでいるとみなした計算結果では説明できない。Li、川添ら [115] による 3-DB 構造に関する第一原理計算は実験を非常によく再現し、第二層の

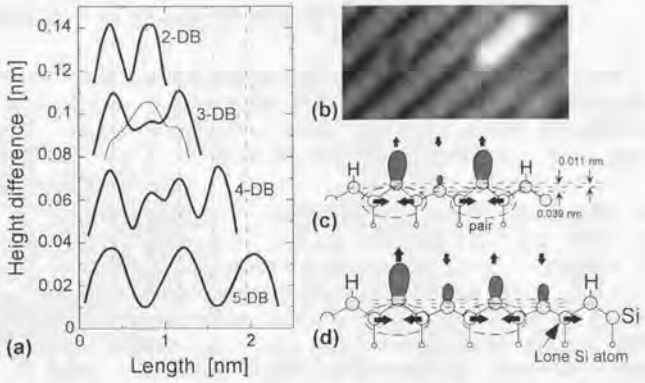

Figure A.2: (a)DB 構造の断面図。太線は占有状態、細線は非占有状態をあらわす。(b)3-DB 構造の STM 像 (4 nm×2 nm, V_s=-2.0 V, I_t=20 pA, 96 K)。(c)3-DB 構造の最安定構造。(d)4-DB 構造の最安定構造の一つ。楕円は DB をあらわし、矢印が原子の変位方向をあらわす。

Si 原子が重要な働きをすることが明らかになった。第二層の原子は図 2(c) に示すように交互に左右に変位してペアを作る傾向があり、それに伴い第一層 Si 原子が突きだすか、または沈む。このとき、突きだした原子の電子エネルギー準位が低くなり、沈んだ原子の電子が突き出した原子に移動することがわかった。

偶数個の DB からなる構造の場合、計算から得られた二つの最安定構造が時間的にフリップしていることがわかった。2 個の DB からなる構造の場合、フリップする時のバリアは 82 meV 程度と見積もられた。しかし 4-DB 構造では、フリッピングバリアは 450 meV 程度であり、100 K 付近ではバリアを越えることができず、最安定構造をとることが期待される。しかし、実験ではフリッピングを示唆する結果が得られた。偶数個の場合は一つの第 2 層原子がペアを作ることができない (4-DB 構造の場合を図 2(d) に示す) が、ペアの組み替えが起きることにより、ペアを作らない原子が実効的に移動してバリアが下がると予測される。さらに、40 K での実験により、このフリッピングが停止することが確かめられた。したがって偶数個の場合、ソリトンのような働きをする原子を通じて、構造が時間的に変化すると結論した。これらの DB 構造は擬分子と見なすことができ、その緩和はヤーンテーラー変形と解釈することができる。

吸着ポテンシャルエネルギーの空間分布観察

低温において水素終端Si(100)2×1表面にGa原子を吸着してSTM観察した結果、Ga原子が一次元的に拡散していると考えられる棒状の構造(図3(a))を見いだした(今後Ga barと呼ぶ)[128]。このGa barは100K付近(現在のまでのところ、77Kから110K)の狭い温度領域でのみ観察され、39K、200K、室温では観測されない。

第一原理計算より得られた、水素終端表面上のGa原子に対する吸着PES[127]を図3(b)に示す。二つのシリコンダイマー列間が最もエネルギーが低くなっており、STM像でGa barが存在する位置と一致している。このPESに基づいて、Ga原子が隣の安定位置に飛び移る確率を求めたところ、ダイマー列を横切る方向に飛び移る確率は非常に小さく、100Kでは一次元方向にのみ移動することも確かめられた。以上のことからGa barは一次元的に運動しているGa原子をSTM観察した結果と結論づけられる。両端のダイハイドライドが井戸型ポテンシャルの壁となっていることがSTM像からわかり、実際に第一原理計算でもダイハイドライドが600meVの壁となっていることがわかった。

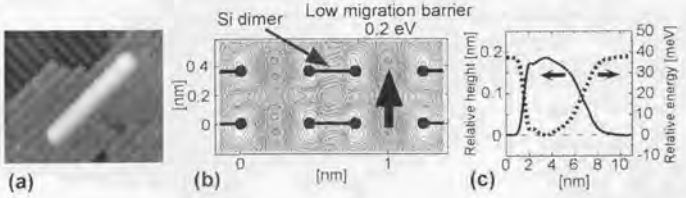

Figure A.3: (a)Ga barのSTM像(12nm×9nm, V_s=-2.0V, I_t= 20pA, 100K)。(b)吸着PESの第一原理計算結果。等高線の間隔は0.1eV。(c)高さが徐々に減るGa barの断面図と吸着エネルギー差。

ポテンシャル井戸に閉じ込められて、一次元ランダムウォークしているGa原子が各ホッピングサイトを訪れる回数は、ポテンシャル井戸の長さに逆比例する。また、STMで観察されるGa barの高さは、探針直下にGa原子が訪れる回数を反映している。したがって、長い井戸に閉じ込められたGa原子ほどSTM探針直下を訪れる回数が少なくなり、低く観察されることが期待される。実際、実験では長いGa barほど低く観察されている。さらに、STM探針とGa原子の間の相互作用について詳細な検討を行った結果、本実験で観測される相互作用は吸着ポテンシャルエネルギー差の議論に影響を及ぼさないことがわかった。これらの結果から、STMはGaの存在確率を直接観測でき、同一Ga bar内での高さの違いから、吸着ポテンシャルエネルギー

の差を定量的に導けることを示した。

実験では高さが徐々に減っていく Ga bar も観察されている。図 3(c) はその STM 像の断面図と、断面の最高点をゼロ点とした時の各サイトの吸着ポテンシャルエネルギー差を表している。この結果から数 nm オーダーで空間的にポテンシャルが変化していることがわかった。STM 像を詳細に検討し、さらに不純物原子のクーロン力が 3 nm から 4 nm に及ぶことを考慮した結果、この空間的変化の原因は表面のステップやシリコン欠陥ではなく、最表面以下の不純物原子または格子欠陥であると結論した。不純物原子の種類については現在検討中である。

結論

微細な領域の表面物性について議論した。将来原子レベルの細線を作ると、細線内で構造安定化が起きて半導体的になる事を初めて指摘し、ある程度のランダムネスが必要であると結論した。また、ダングリングボンド構造のフリッピングバリアの低下にはソリトン的な原子が重要な役割を担っていることを明らかにした。細線を作る際のプロセスにおいては表面の吸着ポテンシャルエネルギーの理解が不可欠である。本研究から、最表面以下の不純物原子または欠陥が表面の吸着ポテンシャルエネルギーに影響を与えている可能性があることがわかった。これは薄膜成長過程の理解に関連して重要な知見に発展すると思われる。

Taro Hitosugi

PUBLICATION LIST

as of February 8, 1999

T. Hitosugi, T. Hashizume, S. Heike, S. Watanabe, Y. Wada, T. Hasegawa and K. Kitazawa,
"Scanning Tunneling Spectroscopy of dangling-bond wires fabricated on the Si(100)-2x1-H surface," Jpn. J. Appl. Phys. **36**, L361-L364 (1997).

T. Hitosugi, T. Hashizume, S. Heike, Y. Wada, S. Watanabe, T. Hasegawa and K. Kitazawa,
"Scanning tunneling spectroscopy of dangling-bond wires fabricated on the Si(100)-2x1-H surface," Appl. Phys. **A66**, S695-S699 (1998).

T. Hitosugi, T. Hashizume, S. Heike, H. Kajiyama, Y. Wada, S. Watanabe, T. Hasegawa and K. Kitazawa,
"Scanning Tunneling Microscopy of Atomic-scale Dangling-bond Structures Fabricated on the Si(100)-2×1-H Surface," J. Surf. Anal. **4**, 312-315 (1998).

T. Hitosugi, T. Hashizume, S. Heike, H. Kajiyama, Y. Wada, S. Watanabe, T. Hasegawa and K. Kitazawa,
"Scanning tunneling microscopy/spectroscopy of dangling-bond wires fabricated on the Si(100)-2x1-H surface," Appl. Surf. Sci. **130-132**, 340-345 (1998).

T. Hitosugi, T. Hashizume, S. Heike, H. Kajiyama, Y. Wada, S. Watanabe, T. Hasegawa and K. Kitazawa,
"Electronic structures of dangling-bond structures fabricated on hydrogen-terminated Si(100)-2×1 surface," in *Defects and diffusion in semiconductor surface* (Scitec Publications, 1998) in press.

Taro Hitosugi, S. Heike, T. Onogi, T. Hashizume, S. Watanabe, Z. -Q. Li, K. Ohno, Y. Kawazoe, T. Hasegawa, and K. Kitazawa
"Jahn-Teller distortion in dangling-bond linear-chains fabricated on a hydrogen-terminated Si(100)-2×1 surface," submitted to Phys. Rev. Lett.

T. Hitosugi, Y. Suwa, S. Heike, T. Onogi, S. Matsuura, S. Watanabe, T. Hasegawa, K. Kitazawa, and T. Hashizume
"Direct observation of one-dimensional Ga-atom migration on Si(100)-2×1-H surface: a local probe of adsorption energy variation," in preparation.

その他

T. Hashizume, S. Heike, T. Hitosugi, S. Watanabe, M. Ichimura, and T. Onogi,
"Fabrication of atomic Ga wires on Si surface and its property," Surface Science **19**, 716-721 (1998).
---in Japanese ---
橋詰富博・平家誠嗣・一杉太郎・渡邊 聡・市村雅彦・小野木敏之：
「走査プローブ顕微鏡を用いた10ナノメートルレベルリソグラフィー」，表面科学 **19**, 716-721 (1998).

T. Hashizume, S. Heike, T. Hitosugi and K. Kitazawa,
"Application of atom manipulation for fabricating nanoscale and atomic-scale structures on the Si surfaces," T. Sakurai Ed. In *New Materials Science Series* (Springer-Verlag Heidelberg, 1998) in press.

物理学会誌表紙 1998 年 6 月号　STM 像提供

日経産業新聞 1998 年 5 月 26 日　STM 像提供

日刊工業新聞 1999 年 1 月 12 日　科学技術面　記事

H. Kajiyama, S. Heike, T. Hitosugi, and T. Hashizume,
"Initial Backbond Oxidation at an Unpaired Dangling Bond Site on a hydrogen-terminated Si(001)-2x1 Surface," Jpn. J. Appl. Phys. Lett. **37**, L1350-L1353 (1998).

H. Kajiyama, S. Heike, T. Hitosugi, and T. Hashizume,
"Fabrication of Silicon Oxide Nano-Wire on a Hydrogen Terminated Si(100)2x1 Surface," submitted to Appl. Phys. Lett.

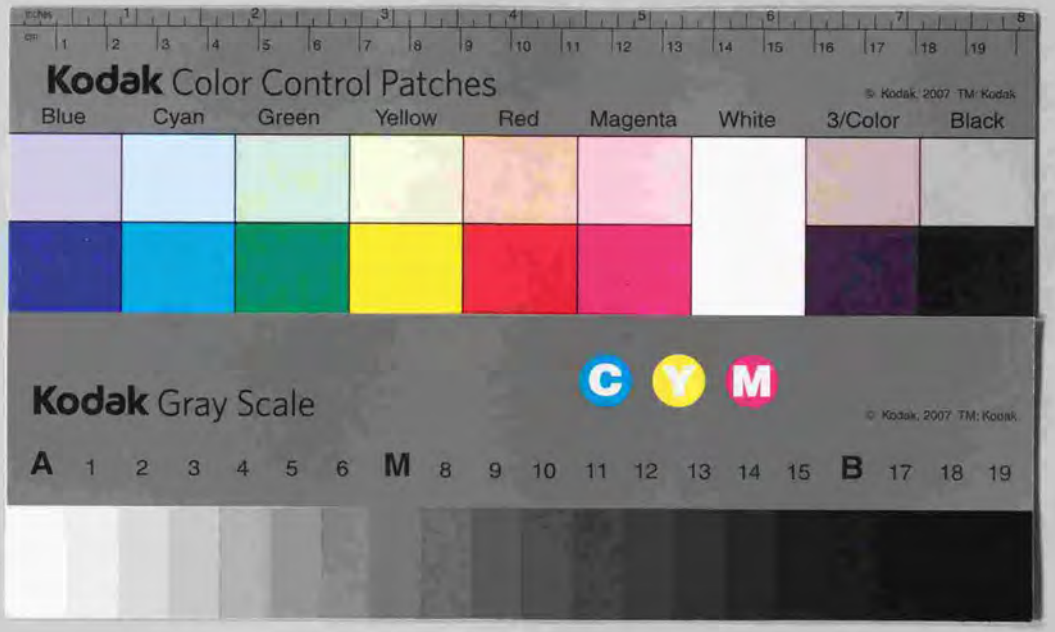
Kodak Color Control Patches
© Kodak, 2007 TM: Kodak
Blue
Cyan
Green
Yellow
Red
Magenta
White
3/Color
Black
Kodak Gray Scale
C
Y
M
© Kodak, 2007 TM: Kodak
A 1 2 3 4 5 6 M 8 9 10 11 12 13 14 15 B 17 18 19